International Journal of Solids and Structures 000 (2017) 1–17

Contents lists available at ScienceDirect

International Journal of Solids and Structures

journal homepage: www.elsevier.com/locate/ijsolstr

Elasto-plastic contact of materials containing double-layered inhomogeneities

Mengqi Zhang[a,b], Ning Zhao[a,*], Peter Glaws[c], Phil Hegedus[c], Qinghua Zhou[d], Zhanjiang Wang[e], Xiaoqing Jin[f], Leon M. Keer[b], Qian Wang[b,e,*]

[a] School of Mechanical Engineering, Northwestern Polytechnical University, Xi'an 710072, China
[b] Center for Surface Engineering and Tribology, Northwestern University, Evanston, Illinois 60201, USA
[c] TimkenSteel, Canton, Ohio 44706, USA
[d] School of Aeronautics and Astronautics, Sichuan University, Chengdu 610065, China
[e] Department of Mechanical Engineering, Southwest Jiaotong University, Chengdu 610031, China
[f] State Key Laboratory of Mechanical Transmission, Chongqing University, Chongqing 400030, China

ARTICLE INFO

Article history:
Received 1 March 2017
Revised 5 August 2017
Available online xxx

Keywords:
Elasto-plastic contact
Plastic strain concentration
Double-layered inhomogeneities
Numerical equivalent inclusion method

ABSTRACT

Double-layered inhomogeneities consist of enclosed, or layered, inhomogeneities of different material properties, embedded in a matrix material. They are found in engineering materials used for components under contact and relative motion. Currently, most theoretical investigations on the double-layered inhomogeneities are limited to elastic or plane-strain problems. This work proposes a novel model, based on the numerical equivalent inclusion method, for the elasto-plastic contact of materials with double-layered inhomogeneities. The current analysis is focused on such inhomogeneities as a stiff core enclosed by a compliant outer layer. A group of in-depth parametric studies is performed to reveal the effects of this type of double-layered inhomogeneities on the contact plasticity of the matrix material. The results indicate that the plastic strain distribution in the matrix material is related to the Young's modulus and geometric eccentricity of the inner and outer inhomogeneities, as well as the location and shape of the inhomogeneities. For the cases of individual double-layered inhomogeneity embedded at different locations, the maximum equivalent plastic strain in the matrix appears in the vicinity of the double-layered inhomogeneity, wherever is the closest to the location of the theoretical maximum elastic stress from the homogeneous solution. For the cases of multiple double-layered inhomogeneities, the overlap of the plastic strain concentration regions amplifies the disturbance caused by these inhomogeneities, and the amplification effect is related to the inhomogeneity layout. If the stiff core is completely encircled in the outer inhomogeneity layer, plastic strains would initiate from the outer layer and then permeate to the matrix material.

1. Introduction

An inhomogeneity is defined as the subdomain of a material, whose mechanical properties are different from those of the major portion of the material, known as the matrix (Mura, 1987). Inhomogeneities inevitably exist in many engineering materials, such as steels. These materials are widely used in industries to build components subjected to high stresses while working under contact and relative motion. The inhomogeneities may act as the sites for fatigue-crack nucleation and weaken the fatigue strength of materials (Atkinson and Shi, 2003; Li et al., 2014; Sun et al., 2013; Zhang et al., 2013). Some inhomogeneities appear in the form of double-layered structures composed of enclosed inhomogeneities of different material properties (Byun et al., 2003; Zhang et al., 2016), as Fig. 1 shows. Apparently, such an inhomogeneity could result in different mechanical impact to the material than does a homogeneous inhomogeneity. This inspires the authors to study the micromechanics nature of double-layered inhomogeneities.

The rolling contact fatigue life of mechanical components is significantly affected by inhomogeneities. Their existence can induce material microstructure variations, for example, the formation of butterfly wings, when the material is subjected to cyclic rolling contact loading (Moghaddam and Sadeghi, 2016). Micro cracks initiated around an inhomogeneity may propagate to the surface and finally result in contact surface failure. In spite of some controversial issues, a number of studies have pointed out that the effect of

* Corresponding authors.
E-mail addresses: mengqi.zhang@mail.nwpu.edu.cn, zhangmq1989@gmail.com (M. Zhang), zhaon@nwpu.edu.cn (N. Zhao), qwang@northwestern.edu (Q. Wang).

http://dx.doi.org/10.1016/j.ijsolstr.2017.08.006
0020-7683/

Nomenclature

a_0	Hertz contact radius
a_1, a_2, a_3	element size along the x, y and z directions, respectively
B, c, n	material constants for the isotropic hardening law
C^*_{ijkl}, C_{ijkl}	coefficients of elastic properties for inhomogeneity and matrix, respectively
ΔD_{ijkl},ΔH_{ijkl}	coefficients, where $\Delta D_{ijkl} = (C^{*-1}_{ijkl} - C^{-1}_{ijkl})$,$\Delta H_{ijkl} = C^{-1}_{ijmn}(C_{mnkl} - C^*_{mnkl})$
D^E_{ijk}	influence coefficients relating contact pressure and subsurface elastic stress
D^R_{ijkl}	influence coefficients relating plastic strain and subsurface residual stress
E	Young's modulus
h	total gap between contact surfaces
h_0	initial gap (no deformation) between contact surfaces
I_g	set of all elements in the grid
I_c	set of the elements in the contact area
K	influence coefficients relating contact pressure and surface elastic displacement
K^R_{ijk}	influence coefficients relating plastic strain and surface residual displacement
N_x, N_y, N_z	total element number along the x, y and z directions, respectively
P_0	Hertz contact pressure
p	contact pressure
S_{ij}	deviatoric stress
$T^{(0)}_{ijkl}$, $T^{(1)}_{ijkl}$, $T^{(2)}_{ijkl}$, $T^{(3)}_{ijkl}$	influence coefficients relating eigenstrain and eigenstress
u_3	normal elastic surface displacement
u^R_3	normal residual surface displacement
W	total normal load
α, β, γ	element indices number along the x, y and z directions, respectively
ξ, η, ϑ	element indices number along the x, y and z directions, respectively
ε^P_{ij}	plastic strain
ε^*_{ij}	eigenstrain
ε^H_{ij}	sum of strains from homogeneous solution
ε^P_{Eq}	equivalent plastic strains
ε_{ij}	total strain used in the equations of the numerical equivalent inclusion method
$\varepsilon^{(1)}_{ij}$, $\varepsilon^{(2)}_{ij}$	components of ε_{ij}, i.e. $\varepsilon_{ij} = \varepsilon^{(1)}_{ij} + \varepsilon^{(2)}_{ij}$
λ	effective accumulative plastic strain
ν	Poisson's ratio
σ^E_{ij}	contact-induced initial subsurface elastic stress
σ^R_{ij}	residual stress
σ^*_{ij}	disturbance stress (eigenstress)
σ_{VM}	von Mises stress
σ_Y	yield strength
ω	rigid-body motion

inhomogeneities on rolling contact fatigue was driven by complicated reversal stresses and strains around them (Moghaddam et al., 2014, 2015) . Therefore, the stress-strain analysis is the very first step to examine the link between inhomogeneities and rolling contact fatigue.

Usually, mechanical components are designed to operate within the elastic range based on the assumption that the materials are homogeneous. However, heterogeneous cyclic plasticity at the microstructural scale can be induced by high and localized stresses due to inhomogeneities. Such micro-plasticity raises concerns in rolling contact fatigue and thus has attracted a great deal of attention. For example, the fatigue indicator parameters (FIPs) related to the maximum plastic strain range or other properties, were developed to connect local cyclic plasticity to the drivers for fatigue crack formation (Fatemi and Socie, 1988; Zhang et al., 2009; Przybyla et al., 2010). Pandkar et al., (2014) investigated the participation of carbides in the plastic deformation accumulation in case-hardened M50-NiL bearing steel under a rolling contact load and observed hardness to increase within the RCF-affected zone. The hardness changes somewhat reflected the microstructural variation in this rolling-contact fatigue process (Bhattacharyya et al., 2014).

A number of microstructure-sensitive models have been developed for analyzing material heterogeneities by means of the finite element method (FEM) and the semi-analytical method (SAM). The FEM has good flexibility and versatility for handling complicated situations. However, three-dimensional (3D) FEM contact modeling requires a large solution domain (at least ten times the contact region in each dimension) and very fine mesh, and its execution is time consuming. The SAM, on the other hand, does not require a large solution domain because it is built upon analytical core solutions; it has been proven convenient for solving contact problems. SAM is especially suitable for implementing the idea of the equivalent inclusion method (EIM), proposed by Eshelby (1957), that converts an inhomogeneity problem to an inclusion problem accompanied with prescribed eigenstrains. Based on Mura (1987), inclusions are eigenstrain-containing sub-domains whose properties are identical to those of the matrix. Examples of eigenstrains are thermal expansion, plastic strain, and magneto-mechanical strain. Two steps are needed when utilizing the EIM to solve an inhomogeneity problem, which are 1) replacing inhomo-

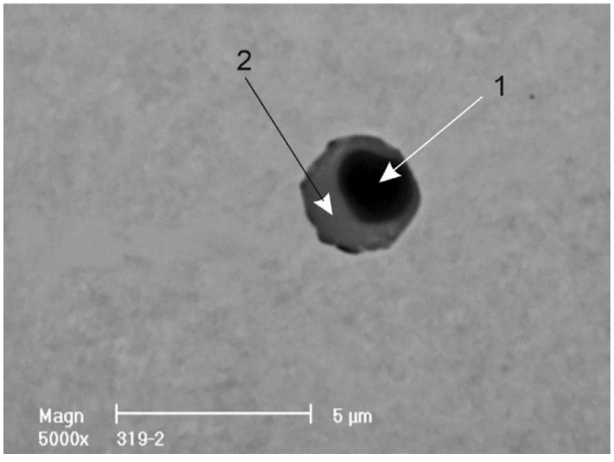

Fig. 1. Scanning Electron Microscope image of a double-layered inhomogeneity microstructure in a steel (Lis, 2009). 1– Aluminum oxide, 2– Manganese sulfide.

Please cite this article as: M. Zhang et al., Elasto-plastic contact of materials containing double-layered inhomogeneities, International Journal of Solids and Structures (2017), http://dx.doi.org/10.1016/j.ijsolstr.2017.08.006

geneities by equivalent inclusions that contain properly assigned eigenstrains under the condition that the stress fields induced by equivalent inclusions equal those by inhomogeneities, and 2) calculating the stress distributions caused by the eigenstrains thus imposed. The EIM, combined with the elastic stress solutions of ellipsoidal inclusions (Eshelby, 1957), has led to many studies and method developments. For example, Zhou et al., (2014a) proposed a highly efficient approximate method to treat problems involving distributed ellipsoidal inhomogeneities in a 3D half-space. This model was further used to investigate the effects of reinforcing particles on the rolling fatigue lives of (TiB + TiC)/Ti-6Al-4 V composites (Zhou et al., 2014b).

In recent years, the idea of EIM has been extended to the numerical equivalent inclusion methodology (NEIM), in order to analyze the inhomogeneities that have irregular shapes (Liu and Wang, 2005; Liu et al., 2012; Koumi et al., 2014; Zhou et al., 2011, 2012, 2015; Amuzuga et al., 2016). With the NEIM, inhomogeneities can be discretized into cubic elements. The stress fields caused by nuclei of strain can be expressed by the basic Galerkin vectors (Yu and Sanday, 1991) and its cuboidal solutions have been solved as closed-form explicit integral kernels for convolution and correlation operations in favor of the fast solution by means of the fast Fourier transform (FFT) (Liu et al., 2000; Liu and Wang, 2002). Wang et al., (2013b) proposed a more efficient method to calculate the eigenstress, in which parallel computing technologies were also utilized to boost the computational efficiency. A thorough summary of the recent research on inclusion related problems can be found in the review by Zhou et al., (2013). The efforts on coupling multiple stress fields and contact elasto-plasticity also deserve mentioning. For example, Wang et al., (2013a) extended the partial-slip contact model to inhomogeneous materials by utilizing the NEIM approach mentioned above. Most recently, Amuzuga et al., (2016) analyzed the influence of inhomogeneities on the stress and strain fields of an elasto-plastic half-space. Dong et al., (2016) constructed a coupled model to consider elasticity, plasticity, inhomogeneity, and partial slip in contact of materials.

However, models and solutions to the contact of materials involving double-layered inhomogeneities are rarely seen in the works mentioned above. A double-layered inhomogeneity microstructure is referred to a set of two inhomogeneities of different materials, one surrounded by the other, as shown in Fig. 1. In steels, the core of a double-layered inhomogeneity is usually a stiff particle, such as an oxide or nitride, while the outer layer may be a complaint sulfide of much higher deformability. The research aims to develop a SAM based elasto-plastic contact model for the analyses and numerical simulations of the plasticity behaviors of double-layer inhomogeneities, and to conduct in-depth parametric studies for quantifying the influence of a double-layered inhomogeneity on the plasticity of its surrounding steel material.

2. Elasto-plastic contact of inhomogeneous materials

2.1. Problem description

Fig. 2 presents the contact between an inhomogeneous half-space and a rigid indenter. A concentrated force, W, is applied on the indenter. The calculation zone is expressed in a Cartesian coordinate system, where the x- and y- axes are parallel to the surface of the half-space and the z-axis points to depth direction. The origin, O, of the coordinate system is at the center of the contact area. The half-space is elasto-plastic and contains several inhomogeneities including double-layered ones. The entire calculation zone is discretized into $Nx \times Ny \times Nz$ cubic elements. The inhomogeneity shape is not limited to ellipsoidal, and multiple material components can be readily involved. Material properties are

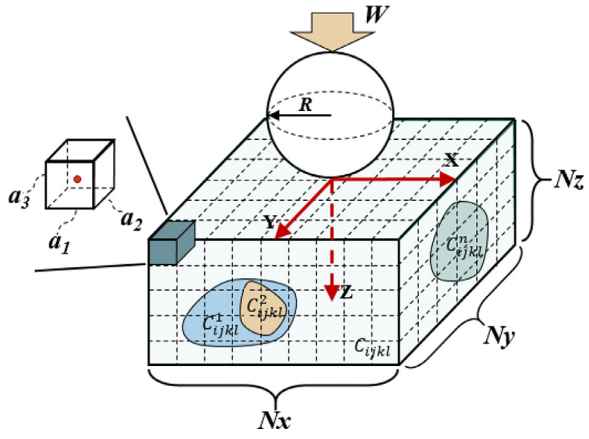

Fig. 2. Inhomogeneous material subjected to contact loading. A double-layered inhomogeneity set (front) and a uniform inhomogeneity (side) are shown. The element at the top left corner of the half space is enlarged to view the definition of an element by its edges, a_1, a_2, and a_3.

assigned to each element corresponding to inhomogeneities or the matrix. Although Fig. 2 describes a general scenario, the current research will focus on double-layered inhomogeneity cases.

Four procedures should be performed when using the current model: 1). Determination of the contact pressure between the indenter and the half-space; 2). Calculation of the subsurface elastic stress field when the contact pressure is determined; 3). Solution of the eigenstress caused by inhomogeneities; and 4). Evaluation of plastic strains and residual stresses, as well as the residual displacement of the surface.

2.2. Inhomogeneity consideration

2.2.1. Governing equations for the numerical equivalent inclusion method

As mentioned, the mechanical properties of an inhomogeneity are different from those of the major portion of the material system, known as the matrix, while an inclusion has the same properties as those of the matrix but contains eigenstrains, as defined by Mura (1987). Sometimes, an inhomogeneity may also have a distributed internal eigenstrain and is termed as the inhomogeneous-inclusion (Mura, 1987). In this paper, the pre-described eigenstrain inside an inhomogeneity is referred to as plastic strain.

Following the EIM (Eshelby, 1957), an inhomogeneity is replaced by an inclusion, as a convenient stepping stone, by choosing an equivalent eigenstrain distribution ε^*_{ij} that enables the EIM to result in a stress field identical to that of the original problem. The consistency condition of the EIM for inhomogeneous-inclusion problems, which is enforced in each element, is shown as:

$$C^*_{ijkl}\left(\varepsilon^E_{kl} + \varepsilon_{kl} - \varepsilon^P_{kl}\right) = C_{ijkl}\left(\varepsilon^E_{kl} + \varepsilon_{kl} - \varepsilon^P_{kl} - \varepsilon^*_{kl}\right) \text{in}\Omega \quad (1)$$

where, C^*_{ijkl} and C_{ijkl} are the elastic coefficients of inhomogeneity and matrix, respectively, ε^E_{ij} is the elastic strain corresponding to the homogeneous solution of the contact-induced elastic stress σ^E_{ij}, ε^P_{ij} the plastic strain, ε^*_{ij} the equivalent eigenstrain, and ε_{ij} the strain disturbance caused by inhomogeneous-inclusions (Mura, 1987).

Based on the EIM theory (Mura, 1987), disturbance strains ε_{ij} are linearly related to eigenstrains. The plastic strain is considered as one kind of eigenstrain. The right side of Eq. (1) implies that for an inhomogeneous-inclusion problem, the total eigenstrain of the equivalent inclusion contains two portions, plastic strain ε^P_{ij} and equivalent eigenstrain ε^*_{ij}. Therefore, disturbance strain ε_{ij} can be expressed as the sum below, in order to separate the unknownε^*_{ij}:

Please cite this article as: M. Zhang et al., Elasto-plastic contact of materials containing double-layered inhomogeneities, International Journal of Solids and Structures (2017), http://dx.doi.org/10.1016/j.ijsolstr.2017.08.006

$$\varepsilon_{ij} = \varepsilon_{ij}^{(1)} + \varepsilon_{ij}^{(2)} \tag{2}$$

where $\varepsilon_{ij}^{(1)}$ and $\varepsilon_{ij}^{(2)}$ are linearly depend on ε_{ij}^{P} and ε_{ij}^{*}, respectively. Substituting Eq. (2) into (1) results in:

$$\begin{aligned} &C_{ijkl}^{*}\left[\left(\varepsilon_{kl}^{E} + \varepsilon_{kl}^{(1)} - \varepsilon_{kl}^{P}\right) + \varepsilon_{kl}^{(2)}\right] \\ &\quad = C_{ijkl}\left[\left(\varepsilon_{kl}^{E} + \varepsilon_{kl}^{(1)} - \varepsilon_{kl}^{P}\right) + \varepsilon_{kl}^{(2)} - \varepsilon_{kl}^{*}\right] \text{ in } \Omega \end{aligned} \tag{3}$$

Let $\varepsilon_{ij}^{H} = \varepsilon_{ij}^{E} + \varepsilon_{ij}^{(1)} - \varepsilon_{ij}^{P}$, where superscript H means the 'homogeneous solution'. Then Eq. (3) becomes,

$$C_{ijkl}^{*}\left(\varepsilon_{kl}^{H} + \varepsilon_{kl}^{(2)}\right) = C_{ijkl}\left(\varepsilon_{kl}^{H} + \varepsilon_{kl}^{(2)} - \varepsilon_{kl}^{*}\right) \text{ in } \Omega \tag{4}$$

Eq. (3) demonstrates how the plastic strain, ε_{ij}^{P}, is involved with the initial strain state, ε_{ij}^{H}. Equivalent eigenstrain is the only unknown thus Eq. (4) can be solved. The consistency condition Eq. (4) can be reorganized into the following form as a preparation for the numerical implement of the EIM:

$$\varepsilon_{ij}^{*} = \Delta H_{ijkl}\left(\varepsilon_{kl}^{H} + \varepsilon_{kl}^{(2)}\right) \text{ in } \Omega \tag{5}$$

Converting the strains at the right-hand side to the stress format as the following:

$$\varepsilon_{ij}^{*} = \Delta D_{ijkl}\left(\sigma_{kl}^{H} + \sigma_{kl}^{*}\right) \text{ in } \Omega \tag{6}$$

where,

$$\begin{cases} \Delta H_{ijkl} = C_{ijmn}^{-1}\left(C_{mnkl} - C_{mnkl}^{*}\right) \\ \Delta D_{ijkl} = \left(C_{ijkl}^{*-1} - C_{ijkl}^{-1}\right) \end{cases} \tag{7}$$

σ_{ij}^{H} is the initial stress as the summation of contact-induced elastic stress σ_{ij}^{E}=$C_{ijkl}\varepsilon_{kl}^{E}$ and residual stress σ_{ij}^{R}. The residual stress can be expressed as $\sigma_{ij}^{R} = C_{ijkl}(\varepsilon_{kl}^{(1)} - \varepsilon_{kl}^{P})$ by following the basic equation of EIM (Eq. (1)) because the plastic strain is considered as a kind of eigenstrains. However, such an expression is not convenient for numerical calculation; therefore, in this paper, the residual stress and eigenstress are calculated by identical equations expressed as $\sigma_{ij}^{R} = T_{ijkl}\varepsilon_{kl}^{P}$ and $\sigma_{ij}^{*} = T_{ijkl}\varepsilon_{kl}^{*}$. The influence coefficients, T_{ijkl}, will be discussed in Section 2.2.2 in detail.

2.2.2. Eigenstress calculation

The total stress of inhomogeneous-inclusion problems is the superposition of initial stress σ_{ij}^{H} and eigenstress σ_{ij}^{*}. The direct analytical solution of eigenstress derived by Liu et al., (2012) is implemented in this work to avoid truncation error. The eigenstress is expressed as convolutions and correlations of influence coefficients and eigenstrains of any distribution:

$$\begin{aligned} \sigma_{ij}^{*}(\alpha,\beta,\gamma) = \frac{-\mu}{4\pi(1-\nu)}\Bigg(&\sum_{\xi=1}^{Nx}\sum_{\eta=1}^{Ny}\sum_{\vartheta=1}^{Nz} T_{ijkl}^{(0)}(\alpha-\xi,\beta-\eta,\gamma-\vartheta)\varepsilon_{kl}^{*}(\xi,\eta,\vartheta) \\ &+ \sum_{\xi=1}^{Nx}\sum_{\eta=1}^{Ny}\sum_{\vartheta=1}^{Nz} T_{ijkl}^{(1)}(\alpha-\xi,\beta-\eta,\gamma+\vartheta)\varepsilon_{kl}^{*}(\xi,\eta,\vartheta) \\ &+ z\sum_{\xi=1}^{Nx}\sum_{\eta=1}^{Ny}\sum_{\vartheta=1}^{Nz} T_{ijkl}^{(2)}(\alpha-\xi,\beta-\eta,\gamma+\vartheta)\varepsilon_{kl}^{*}(\xi,\eta,\vartheta) \\ &+ z^{2}\sum_{\xi=1}^{Nx}\sum_{\eta=1}^{Ny}\sum_{\vartheta=1}^{Nz} T_{ijkl}^{(3)}(\alpha-\xi,\beta-\eta,\gamma+\vartheta)\varepsilon_{kl}^{*}(\xi,\eta,\vartheta)\Bigg) \end{aligned} \tag{8}$$

where ξ, η, θ and α, β, γ are the element index, Nx, Ny, and Nz the grid numbers of the calculation zone along the x-, y-, and z-direction, and $T_{ijkl}^{(0)}$, $T_{ijkl}^{(1)}$, $T_{ijkl}^{(2)}$ and $T_{ijkl}^{(3)}$ are the influence coefficients and ε_{ij}^{*} are the eigenstrains. Detailed expressions of influence coefficients can be found in the appendix of the reference paper (Liu et al., 2012).

Eq. (8) contains a 3D convolution (the first term) and convolution-correlation combination terms (the remaining three). As described by Liu and Wang (2005) and Liu et al., (2012), the computation of 3D convolution can be accelerated by DC-FFT, while the convolution-correlation terms are evaluated by DC-FFT in the x- and y- directions and the discrete correlation and fast Fourier transform (DCR-FFT) algorithm in the z- direction (Liu et al., 2007; Chen et al., 2008).

The four groups of convolution or convolution-correlation in Eq. (8) can be evaluated separately at the same time. Therefore, a parallel calculation strategy is possible for accelerating the most time-consuming portion of the algorithm (Wang et al., 2013b). Fig. 3 shows the chosen parallel calculation strategy, where each of the four operations is undertaken by a parallel thread, and the results are summed when the calculations of all threads are completed. An open-source software package, named FFTW (http://www.fftw.org/), is employed for performing the fast Fourier transform in the present study. The FFTW can be made parallel as well, implying that more than four threads can be involved in the calculation if necessary.

2.3. Surface contact and elastic stress field

The contact between surfaces is defined by equation system (9), which is then transformed to the frequency domain by the DC-FFT algorithm (Liu et al., 2000; Liu and Wang, 2002) and solved by using a single-loop iteration scheme based on the conjugate gradient method (CGM) (Polonsky and Keer, 1999). The process is briefly mentioned here for clarity.

$$\begin{cases} a_1 a_2 \sum\limits_{(\alpha,\beta)\in I_g} p(\alpha,\beta) = W \\ h(\alpha,\beta) = h_0(\alpha,\beta) + u_3(\alpha,\beta) - \omega \\ p(\alpha,\beta) \geq 0, \quad h(\alpha,\beta) = 0(\alpha,\beta) \in I_c \\ p(\alpha,\beta) = 0, \quad h(\alpha,\beta) \geq 0(\alpha,\beta) \notin I_c \\ u_3(\alpha,\beta) = \sum\limits_{\xi=1}^{Nx}\sum\limits_{\eta=1}^{Ny} K(\alpha-\xi,\beta-\eta)p(\alpha,\beta) \end{cases} \tag{9}$$

where a_1 and a_2 are the sizes of element, ξ and η, α and β the element indices, Nx and Ny the total element number of the calculation zone along the x- and y-directions, and K is the influence coefficients relating the contact pressure to the surface displacement. Eq. (9) involves W, the total normal load, p, the contact pressure, h, the gap between the two surfaces, ω, the rigid-body motion between the two solids, h_0, the initial gap before loading, and u_3, the normal elastic surface displacement. In addition, I_c is the set of all elements that are in contact while I_g is the set of all elements in the grid. The residual plastic surface displacement, once identified, will be added into h_0 and to the real surface roughness data, as well, if available. Note that a rolling contact simulation is achieved by changing the relative location of the indenter with respect to the origin point of the half-space, which can be represented by the initial gap between the contacted surfaces, h_0.

The subsurface elastic stress field, σ_{ij}^{E}, is expressed by the following form of discrete convolution:

$$\sigma_{ij}^{E}(\alpha,\beta,\gamma) = \sum_{\xi=1}^{Nx}\sum_{\eta=1}^{Ny} D_{ij}^{E}(\alpha-\xi,\beta-\eta,\gamma)p(\xi,\eta) \tag{10}$$

where D_{ij}^{E} is the influence coefficients, α, β, γ and ξ, η are the element indices, respectively, and N_x and N_y the element numbers of calculation zone along the x- and y-directions. Detailed expressions of D_{ij}^{E} were given in the work by Liu and Wang (2002).

Please cite this article as: M. Zhang et al., Elasto-plastic contact of materials containing double-layered inhomogeneities, International Journal of Solids and Structures (2017), http://dx.doi.org/10.1016/j.ijsolstr.2017.08.006

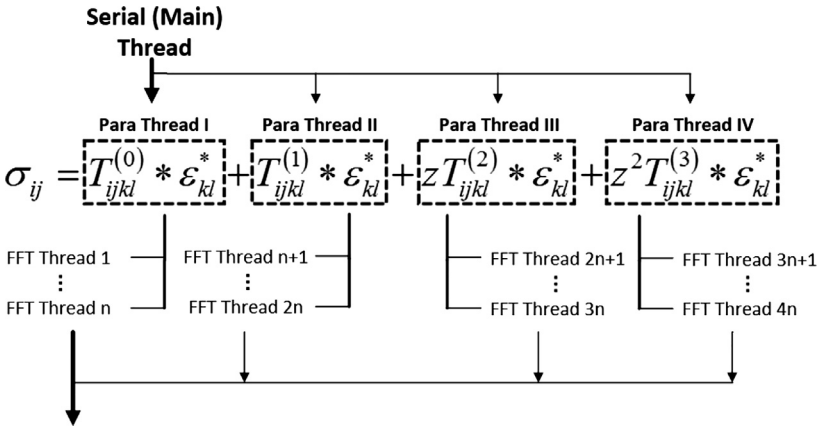

Fig. 3. Parallel calculation strategy. Total computing workload is shared by several threads labeled from I to IV. More threads can be involved when FFTW is parallelized.

2.4. Plasticity consideration

In this work, both the inhomogeneities and matrix materials are considered to be elasto-plastic. The yield strengths and other plasticity-related parameters of the inhomogeneities and the matrix can be different. However, the theory and algorithm that are discussed throughout this section should be applicable to both the matrix and the inhomogeneities. Thus, the parameters in the following paragraphs are not distinguished by material.

Work hardening. Isotropic hardening following the Swift law is considered in the current work to describe the growth of yield strength:

$$\sigma_Y = g(\lambda) = B(c+\lambda)^n \tag{11}$$

where σ_Y is the yield strength, B, c and n are the work hardening parameters related to materials, and $\lambda = \sum d\lambda = \sum \sqrt{2d\varepsilon^p_{ij} : d\varepsilon^p_{ij}/3}$ is the effective accumulative plastic strain.

Yield function. The von Mises yield criterion is utilized to identify yield. The total von Mises stress is the result of superposition of elastic stress σ^E_{ij}, residual stress σ^R_{ij}, and eigenstress σ^*_{ij} that caused by the inhomogeneities, expressed as $\sigma_{VM} = \sigma^E_{ij} + \sigma^R_{ij} + \sigma^*_{ij}$. The yield function is:

$$f = \sigma_{VM} - \sigma_Y = \sqrt{\frac{3}{2} S_{ij} : S_{ij}} - g(\lambda) \tag{12}$$

where $S_{ij} = \sigma_{ij} - \frac{1}{3}\sigma_{kk}\delta_{ij}$ is the deviatoric stress.

Plastic strain increment. The material yields when $f(\lambda) > 0$, i.e. when the von Mises stress is larger than the current yield limit of the material. A new balance is reached if the increment of effective accumulative plastic strain satisfies the condition of $f(\lambda + \Delta\lambda) = 0$. A universal integration algorithm, proposed by Fotiu and Nemat-Nasser (1996) and improved by Nelías et al., (2006), is used to calculate the value of $\Delta\lambda$ for each load step. Finally, the plastic strain increment is determined by the plastic-flow rule that expressed as:

$$\Delta\varepsilon^P_{ij} = \left[\lambda^{(n+1)} - \lambda^{(1)}\right] \frac{3S^{(n+1)}_{ij}}{2\sigma^{(n+1)}_{VM}} \tag{13}$$

Surface residual displacement and residual stress field. According to the work of Jacq et al., (2002), the surface residual displacement, u^R_3, can be expressed as follows based on the reciprocal theorem:

$$u^R_3(\alpha,\beta) = \sum_{\xi=1}^{Nx}\sum_{\eta=1}^{Ny}\sum_{\vartheta=1}^{Nz} K^R_{ijk}(\alpha-\xi,\beta-\eta,\vartheta)\varepsilon^P_{jk}(\xi,\eta,\vartheta) \tag{14}$$

The residual stresses, σ^R_{ij}, are obtained by superposing the contributions of all yield regions with non-zero plastic strain. The residual stress can be calculated through treating the plastic strains as eigenstrains (Liu et al., 2012) by using Eq. (8).

2.5. Flow chart of the overall algorithm

Fig. 4 shows the overall flow chart to solve the contact of elasto-plastic inhomogeneous materials, which consists of two iterations: the numerical EIM (NEIM) loop and the plasticity loop. The NEIM loop, on the basis of the iterative method proposed by Zhou et al. (2015), is utilized to determine the equivalent eigenstrains and corresponding eigenstresses. The plasticity loop pertains to the algorithm developed by Jacq et al., (2002), in which plastic strains, residual stresses, and surface residual displacements are calculated.

The solution starts from a pre-process by dividing the total applied load, W, into several loading steps. In the NEIM loop, the elastic and residual stresses are kept unchanged. The total stress of the ith iteration step is updated by summing the elastic and residual stresses with the eigenstress from the (i-1)th step. Then the equivalent eigenstrain is estimated by using Eq. (5) or (6), and the eigenstress by Eq. (8). The difference of the equivalent eigenstrains between the current and the previous iteration step is compared against convergence criterion. Similarly, the total stress is refreshed at the beginning of each plasticity calculation loop by adding the newest eigenstress portion. Next, the plastic strain increment, residual stress and residual surface displacement are determined. The calculation loop will be returned to the elastic contact module if the pre-set convergence criterion is not satisfied; this is because the contact pressure is affected by the latest surface geometry to which the residual displacement was added.

This algorithm is versatile for analyzing contact problems involving uniform, double-layered, or even multi-layered inhomogeneities. Each element in the model is assigned a marker to identify its composition as matrix or inhomogeneities; different material properties are attached to elements according to their markers. No matter how many types of inhomogeneities are modeled, all inhomogeneity elements are converted to matrix elements with proper equivalent eigenstrains by using Eq. (5) or (6) (depending on inhomogeneities' elastic moduli). Then the eigenstress in the half-space is calculated by gathering the eigenstrain contributions from all elements, and the plasticity-related process can be analyzed sequentially.

Please cite this article as: M. Zhang et al., Elasto-plastic contact of materials containing double-layered inhomogeneities, International Journal of Solids and Structures (2017), http://dx.doi.org/10.1016/j.ijsolstr.2017.08.006

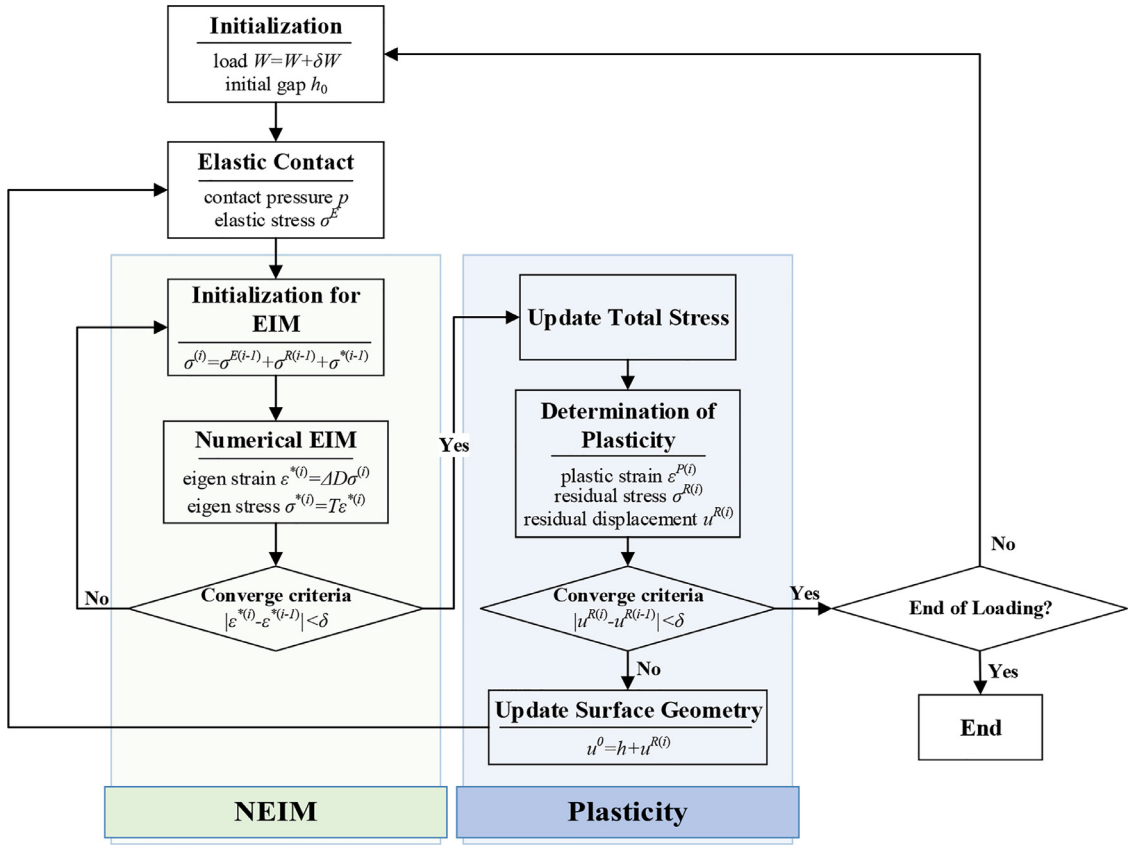

Fig. 4. Flow chart of the algorithm and steps for solving inhomogeneous contact elasto-plastic problems.

Table 1
Parameters of the FE model and new semi-analytical model in validation.

Terms	Matrix	Inner Layer	Outer Layer
Mesh size, FEM		$0.01a_0$	
Mesh size, SAM		$0.04a_0$	
Element number, SAM (x, y, z)		64,64,32	
Location of inhomogeneity center (x, y, z)		$(0, 0, 0.5a_0)$	
Radius of Inhomogeneity r_1, r_2	/	$0.15a_0$	$0.3a_0$
Length of Inhomogeneity l_1, l_2	/	$0.3a_0$	$0.6a_0$
Ratio of Young's Modulus E/E_{Matrix}	1	1.5	0.65
Poisson's Ratio	0.3	0.2	0.2
Initial Yield Strength	$0.3P_0$	/	$0.25P_0$
Hardening Parameter	0.1	/	0.1

2.6. Model validation

The model validation was executed through simulating the contact between a rigid indenter and a half-space containing a short cylindrical double-layered inhomogeneity by the new NEIM model in a reasonably dense mesh and by an axisymmetric FEM model in a very fine mesh set (Table 1). The validation model was so selected that complicated and time-consuming 3D FEM modeling is avoided, while the axisymmetric FEM results can be compared to the 3D results from the current modeling method. The centerline of the double-layered inhomogeneity coincides with the center axis of the indenter. The half-space was partitioned into several sections so that the local refinements of the FEM mesh could be implemented, as shown in Fig. 5(a), while totally 99,690 type CAX4R linear quadrilateral elements were used, hoping that the FEM results thus obtained can be an accurate reference.

In the FEM simulation, the rigid indenter was related to a reference point where the concentrated force was applied. The horizontal displacement and rotation of the indenter were restricted to only indent vertically. The bottom of the half-space was fixed. Both the matrix and outer inhomogeneity are elasto-plastic, while the inner layer is elastic. The Hertz contact radius a_0 and Hertz contact pressure P_0 were used to normalize the geometric terms and stresses, respectively. The major parameters are listed in Table 1. The validation problem involves all key characteristics, such as stiff ($E_I>E_M$) and compliant ($E_I<E_M$) inhomogeneities, and plasticity in both the inhomogeneity (inner layer) and the matrix material. Therefore, the solutions can provide an overall examination of the proposed model.

Fig. 6(a) and (b) plot the equivalent plastic strains solved with the new model and the axisymmetric FEM. The results from the two models are slightly different at the edges of the contours around the inhomogeneity due to the mesh size difference. The stress and plastic strain values along the central axis and the x-axis are compared in Fig. 7, respectively. A good agreement is observed, thus the proposed model is validated.

3. Results and discussion

3.1. Basic contact plasticity behavior of double-layered inhomogeneity

The plastic strain fields in a half-space steel that contains a double-layered inhomogeneity are analyzed in this section to reveal the essential micromechanics behaviors of the materials at the vicinity of the inhomogeneity. Spherical inhomogeneities are

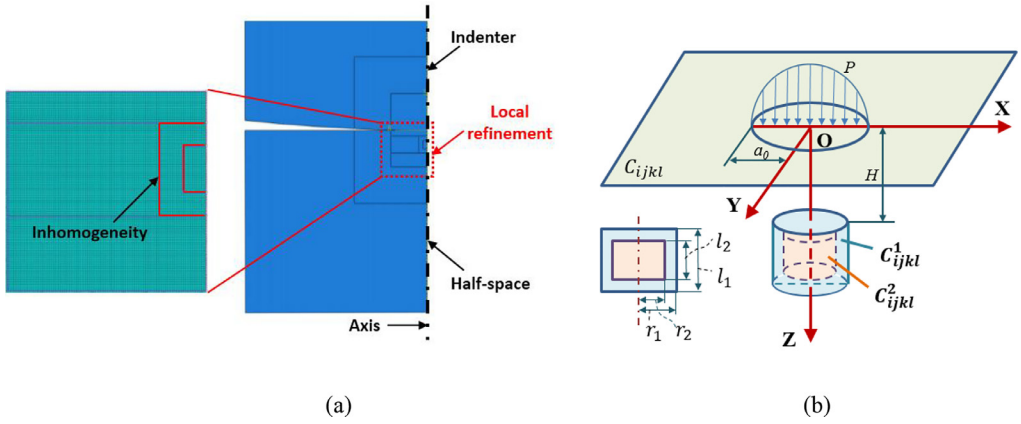

Fig. 5. Model validation: (a) axisymmetric FE model and its local refinements; (b) 3D semi-analytical model.

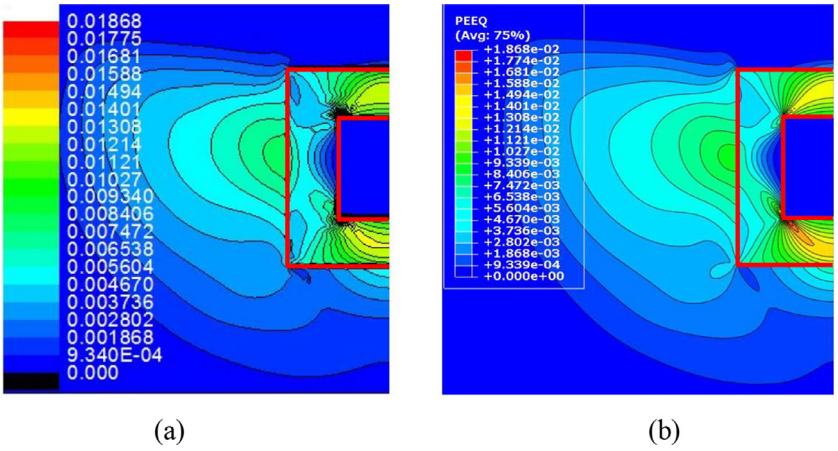

Fig. 6. Results of the equivalent plastic strain solved with (a) the 3D semi-analytical model, (b) the asymmetric FEM.

considered because they are often seen in actual materials. Cases with a uniform stiff or compliant inhomogeneity are also studied for result comparison. The corresponding homogeneous solution is also plotted as a reference. The uniform stiff and compliant inhomogeneities share the same material properties as the inner and outer layers of the double-layered inhomogeneity, respectively. The outer layer is a more compliant inhomogeneity, such as manganese sulfide (MnS), whose elastic modulus is lower than that of the matrix. The inner inhomogeneity core is a stiff particle that can be referred to aluminum oxide (Al_2O_3). The Young's moduli of MnS and Al_2O_3 are 138 GPa and 389 GPa, and their Poisson's ratios are 0.3 and 0.25, respectively (Murakami, 2002a). The hardness of Al_2O_3 is over 2000 HV, implying that it does not yield under the loading condition in current work. Therefore, the core of a double-layered inhomogeneity system is set to be elastic in the following simulations. Matsuno et al., (2006) measured the indentation hardness of MnS. Under the room temperature, the average hardness of MnS is around 150HV. Considering the relationship among yield strength, indentation hardness, Young's modulus, and indenter geometry (Gao et al., 2006), the yield strength of MnS is estimated to be 409 MPa. The matrix properties are selected identical to those reported by Amuzuga et al., (2016) to facilitate comparisons, which are Young's modulus $E_{matrix} = 205$ GPa, Poisson's ratio $\nu = 0.3$, yield strength $\sigma_Y = 730$ MPa, and hardening parameter $n = 0.0095$. The indenter radius and the applied concentrate force are 6 mm and 50 N, respectively, which yield a Hertzian contact radius $a_0 = 100.7$ μm, and the Hertzian contact pressure, P_0, is 2.35 GPa.

The sizes of the inhomogeneities in steels can be found from less than 1 μm to tens of microns (Zhang et al., 2005, 2007; Hashimoto et al., 2011); however, a number of work indicate that large inhomogeneities are more critical to the fatigue resistance of a steel (Murakami, 2002b; Lu et al., 2009; Li, 2012). In the meanwhile, when the inhomogeneity size is comparable to Hertz contact radius a_0, the contact pressure distribution may be significantly affected by inhomogeneities (Leroux et al., 2010; Koumi et al., 2014; Amuzuga et al., 2016; Dong et al., 2016). Therefore, this section focuses on the inhomogeneity of $0.2a_0$ in radius (Amuzuga et al., 2016). For double-layered inhomogeneity, the radius of inner layer is $0.15a_0$. Each inhomogeneity is centered at (0, 0, $0.64a_0$). The equivalent plastic strain (Eq. (15)) is selected to represent the magnitude of plastic strain concentration.

$$\varepsilon^P_{Eq} = \sqrt{\frac{2}{3}\left[\left(\varepsilon^P_{11} - \varepsilon^P_{22}\right)^2 + \left(\varepsilon^P_{22} - \varepsilon^P_{33}\right)^2 + \left(\varepsilon^P_{33} - \varepsilon^P_{11}\right)^2 + 2\left(\left(\varepsilon^P_{12}\right)^2 + \left(\varepsilon^P_{23}\right)^2 + \left(\varepsilon^P_{13}\right)^2\right)\right]} \tag{15}$$

The field of the resulting equivalent plastic strain in the matrix material is of the concern, and Fig. 8 plots its contours in the cross-section XOZ. A pair of circles marks the boundaries between the inner, outer inhomogeneities and the matrix. A contour plot is drawn for $\varepsilon_{Eq}{}^P = 0.55\%$ in Fig. 8 (b-d), which corresponds to the maximum plastic strain encountered in the inhomogeneity-free material, to identify the regions of plastic strain concentrations

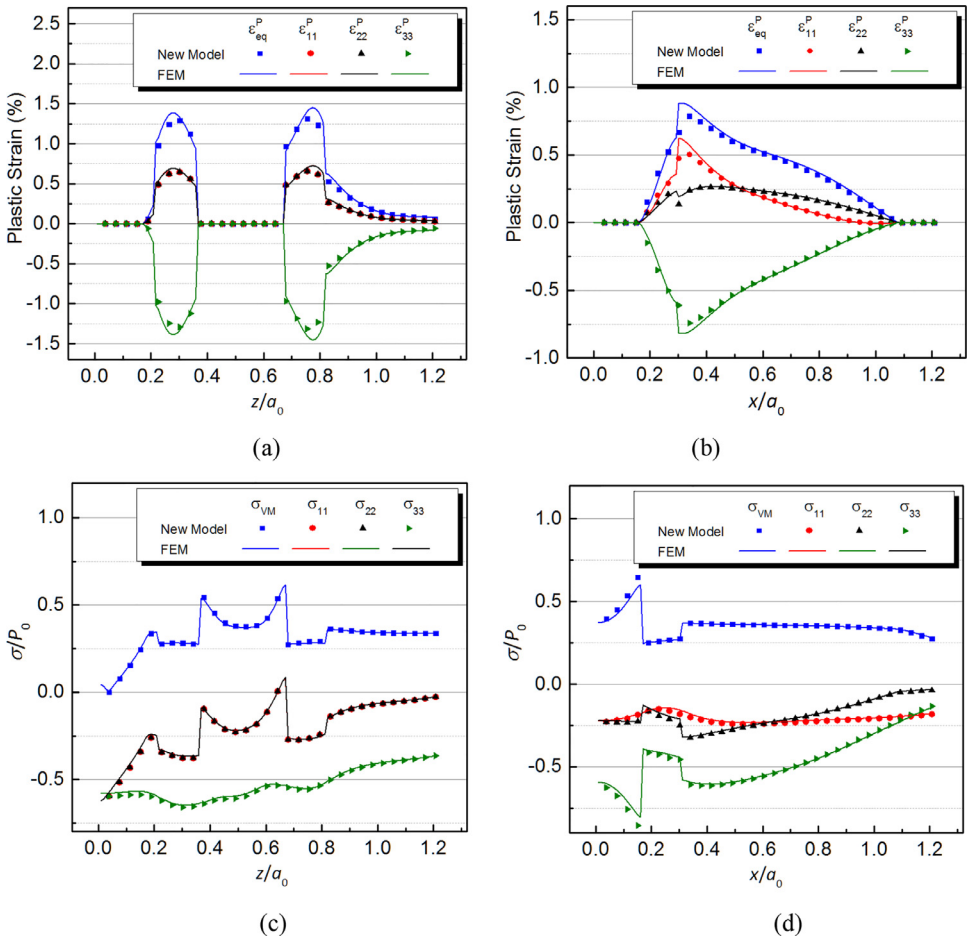

Fig. 7. Plots of the plastic strains (a) along the center line; (b) along the x-axis when $z = 0.5a_0$; Plots of the total stresses (c) along the center line; (d) along the x-axis when $z = 0.5a_0$.

equivalent or more severe than that in Fig. 8(a). Fig. 8(b–d) reveal that plastic strains may concentrate in the two polar areas and the equatorial regions of the spherical inhomogeneity. These regions are marked as I, II, and III, respectively, as shown in Fig. 8(e), for the convenience of further discussion.

The uniform stiff inhomogeneity induces plastic strain concentrations in all these three regions although they are stronger in regions I and II; and the maximum plastic strain in the matrix material is located above the upper boundary of the spherical inhomogeneity. The uniform stiff inhomogeneity causes the highest plastic strain value (1.28%) as compared to other cases in Fig. 8, which is about 2.3 times higher than that in the homogeneous material (Fig. 8(a)). The uniform compliant inhomogeneity results in plastic strain concentrations only in region III; while in regions I and II, the plastic strains are lower than those in the homogeneous case (Fig. 8(a)). The maximum of $\varepsilon_{Eq}{}^P$ in Fig. 8(c) reaches 0.816%, indicating that the compliant inhomogeneity is also a plastic strain raiser although the rise is not as strong as that observed in Fig 8(b). Similar phenomena were reported by Amuzuga et al., (2016) for the uniform inhomogeneity types. Furthermore, when the stiff inhomogeneity core is surrounded by a compliant outer layer, plastic strain concentrations are found in all three regions, as shown in Fig. 8(d). However, compared to the uniform stiff inhomogeneity case, Fig 8(b), the concentration regions I and II around the double-layered inhomogeneity are significantly smaller, and the maximum plastic strain decreases to about 0.99%, implying that the compliant outer layer, to some extent, relieves the plastic strain concentrations caused by the stiff core. Such a buffer effect of the outer layer is related to the material properties and geometric parameters of the inhomogeneities; and therefore, in-depth parametric studies are needed, which are reported in the following sections.

3.2. Parametric studies

3.2.1. Effect of Young's modulus

As mentioned before, in real materials, the inner particle of a double-layered inhomogeneity can be oxide or nitride, such as Al_2O_3 (Lis, 2009), MgO (Chang et al., 2005; Luo et al., 2013), or TiN (Zhang et al., 2016), while the outer layer is usually sulfide. The elastic moduli of different compositions may affect the plastic strain distributions around the double-layered inhomogeneity, and their effects are investigated in this section. The matrix material has Young's modulus $E_{matrix} = 205$ GPa and Poisson's ratio $\nu = 0.3$. The ratio of E_{outer}/E_{matrix} increases from 0.5 to 0.9, while that of E_{inner}/E_{matrix} ranges from 1.0 to 3.0. The Poisson's ratios of the inhomogeneities are set to 0.3 for simplicity. The radii of the spherical outer and inner inhomogeneity are $0.2a_0$ and $0.15a_0$, and the coordinates of inhomogeneity centers are $(0, 0, 0.64a_0)$. Other key parameters, including the size of the indenter and external force, the yield strength of matrix and inhomogeneities, are the same as those used to obtain Fig. 8.

Again, the contour for $\varepsilon_{Eq}{}^P = 0.55\%$ is marked in each subplot in Fig. 9 for identifying the regions of plastic strain concentration equivalent or stronger than that in the homogeneous solution in Fig. 8(a). Fig. 9(a) and (b) plot the equivalent plastic strain in the

Please cite this article as: M. Zhang et al., Elasto-plastic contact of materials containing double-layered inhomogeneities, International Journal of Solids and Structures (2017), http://dx.doi.org/10.1016/j.ijsolstr.2017.08.006

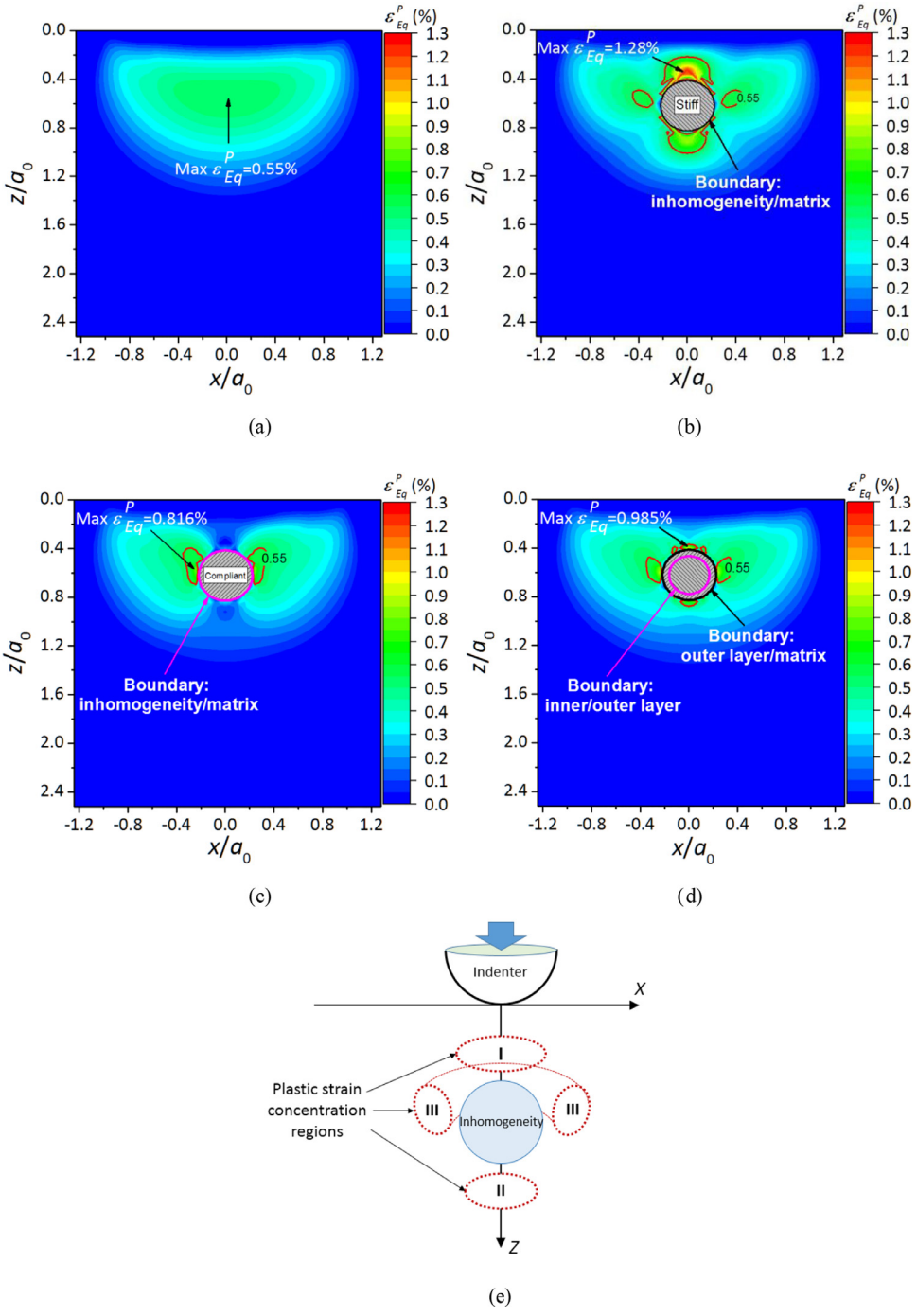

Fig. 8. Equivalent plastic strain distributions in XOZ cross section of (a) a homogeneous half-space, a half-space that contains (b) a uniform stiff inhomogeneity, (c) a uniform compliant inhomogeneity, (d) a double-layered inhomogeneity, under the same point contact loading, and (e) schematic of plastic strain concentration regions.

matrix material with increasing E_{inner}/E_{matrix}, while E_{outer}/E_{matrix} is held constant. In Fig. 9(a) and (b), the plastic strain concentration regions I and II expand with the increase in Young's modulus of the inner inhomogeneity because a harder core induces a stronger disturbance to the plastic strain distribution. Note that the size and shape of region III are barely affected by the change of E_{inner}/E_{matrix}. Thus it can be reasoned that region III is dominated by the compliant outer layer. On the other hand, all three regions are influenced by the increase in Young's modulus of the outer layer, as shown in Fig. 9(c) and (d), where regions I and II expand but region III shrinks. A higher E_{outer}/E_{matrix} causes less disturbance in region III, but the buffer effect of the outer layer is weakened because the other two concentration regions expand, and consequently the maximum equivalent plastic strain in the matrix material increases for over 20%.

Fig. 10 plots detailed plastic strain variations in the vicinities of the individual double-layered inhomogeneity. Two cases with different Young's modulus combinations are considered as representatives, which are $E_{outer}/E_{matrix} = 0.5$ and $E_{inner}/E_{matrix} = 2.0$, and $E_{outer}/E_{matrix} = 0.7$ and $E_{inner}/E_{matrix} = 3.0$. Compared to the results of the homogeneous case, significant deviations of plastic strains are found when the double-layered inhomogeneity appears; however, such disturbances reduce rapidly with increasing distance to the inhomogeneity, either in the depth or the lateral direction.

Please cite this article as: M. Zhang et al., Elasto-plastic contact of materials containing double-layered inhomogeneities, International Journal of Solids and Structures (2017), http://dx.doi.org/10.1016/j.ijsolstr.2017.08.006

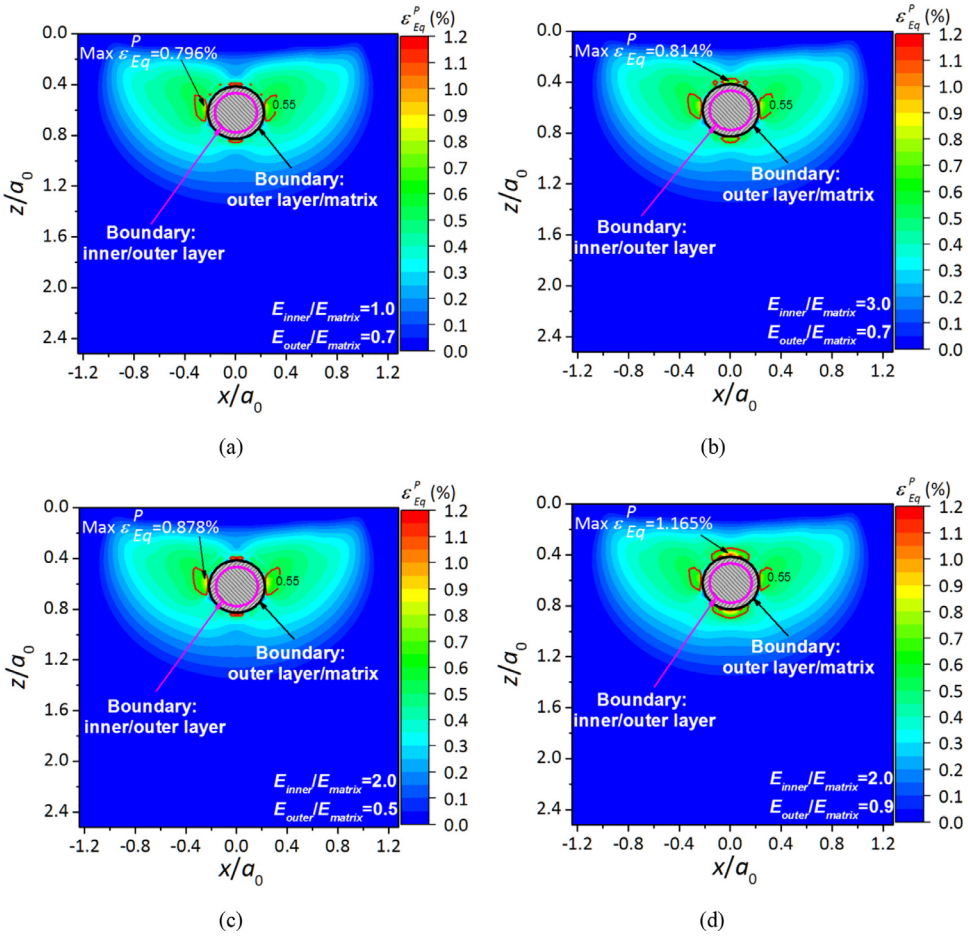

Fig. 9. Equivalent plastic strain fields in cross section XOZ, with varying Young's modulus of (a) (b) the inner layer and (c) (d) the outer layer.

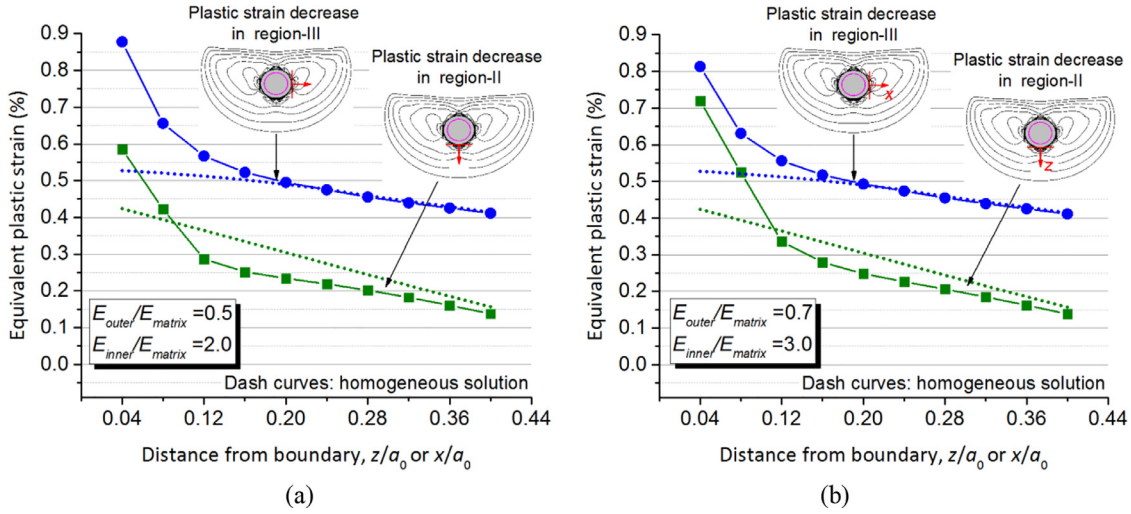

Fig. 10. Variations of the equivalent plasti strains in region II and III for the cases of an individual double-layered inhomogeneity with different Young's moduli.

3.2.2. Effect of inhomogeneity geometries

Size ratio. In real materials, the size of the core of a double-layered inhomogeneity could be either comparable (Fig. 1) or much smaller (Fig. 11) than that of the outer layer. Therefore, the effect of size ratio r_{inner}/r_{outer} on plastic strain distribution in the matrix material is studied, where r_{inner} and r_{outer} are radii of the inner and outer layer of a double-layered inhomogeneity. In this section, r_{outer} is fixed at $0.2a_0$, while r_{inner} is set to be $0.16a_0$ and $0.10a_0$, resulting in size ratios of 0.8 and 0.5, respectively. Young's modulus ratios are set to be $E_{outer}/E_{matrix}=0.7$ and $E_{inner}/E_{matrix}=2.0$, and Poisson's ratios of inhomogeneities are set to be 0.3. Other parameters not specified here are the same as those used in Fig. 8(d). Fig. 12 presents the plastic strain distributions in the matrix material. Regions I and II in Fig. 12(a) are larger than those in Fig. 12(b), suggesting that the buffer effect of the compliant layer is weakened when it is thin. On the other hand, if the stiff core shrinks to $r_{inner}/r_{outer}=0.5$, as shown in Fig. 12(b), the plastic strain distribution caused by this double-layered inhomogeneity is almost the

Please cite this article as: M. Zhang et al., Elasto-plastic contact of materials containing double-layered inhomogeneities, International Journal of Solids and Structures (2017), http://dx.doi.org/10.1016/j.ijsolstr.2017.08.006

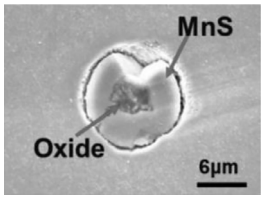

Fig. 11. A double-layered inhomogeneity in steel. The size of the core is much smaller than that of the outer layer (Zhang et al., 2016).

same as that by a uniform compliant inhomogeneity (Fig. 8(c)), where regions I and II disappear, and the location of the maximum plastic strain is in region III. This suggests that a small stiff core can barely affect the plasticity in matrix materials because as Fig. 12(b) shows, regions I and II become smaller when the inner particle shrinks, and these regions are largely encircled by the compliant outer layer; thus the plastic strain concentrations are relieved. This observation suggests that it is reasonable to simplify a double-layered inhomogeneity to a uniform compliant inhomogeneity without losing accuracy if the inner particle is much smaller than the compliant outer layer ($r_{inner}/r_{outer} = 0.5$ or smaller).

Concentricity. In most actual materials, the two layers of a double-layered inhomogeneity may be eccentric (Fig. 13) without center symmetry, and sometimes the stiff core is not totally encircled by the outer layer. Therefore, it is necessary to investigate the concentricity effect of such asymmetric inhomogeneities on plastic strain distributions in matrix materials. For the cases in this section, the outer layer center is fixed at $(0, 0, 0.64a_0)$, while the inner layer center moves along the x- or z-axis until it is tangent to the outer layer. Fig. 14 shows the analysis results for the cases of $E_{outer}/E_{matrix} = 0.7$ and $E_{inner}/E_{matrix} = 2.0$. Poisson's ratios of inhomogeneities are set to be 0.3. Other parameters, including the size of indenter, the external force, the yield strengths of matrix and inhomogeneities, are the same as those used in Fig. 8(d).

Fig. 14(a–c) plot the plastic strain distributions in the matrix material in XOZ section when an eccentric double-layered inhomogeneity exists, and Fig. 14(d) shows the result for the corresponding concentric inhomogeneity case as a reference. The shapes of the plastic strain concentration regions are significantly different in each case. As mentioned before, a stiff inhomogeneity raises plastic strain concentration more in regions I and II, i.e. the north and south poles. When tangent to the outer layer, the stiff core touches the matrix material without any buffer, as shown in Fig. 14(a), resulting in a much larger region I than that in Fig. 14(d) where the core is completely encircled by the complaint outer layer. A similar phenomenon can be observed in Fig. 14(b), where region II expands if the core moves downward. However, the maximum plastic strain in Fig. 14(b) is smaller than that in Fig. 14(a) because the north pole of the stiff inhomogeneity, which should be the location of maximum ε_{Eq}^{P}, is embedded deeper in the compliant outer layer. Thus, the plastic strain concentration in this region is relieved. For the double-layered inhomogeneity in Fig. 14(c), upper and lower regions of strain concentration shift with the stiff core, which results in the highest plastic strain among all the cases in Fig. 14. Meanwhile, the right portion of region III is released because it becomes similar to the situation of Fig. 8(b), and its left equator is similar to that of Fig. 8(c).

Location. In this section, the center location of the double-layered inhomogeneity changes from $0.32a_0$ to $0.8a_0$ along the depth direction, and from 0 to $0.6a_0$ along the x-axis. The Young's moduli of the double-layered inhomogeneity are $E_{outer}/E_{matrix} = 0.7$ and $E_{inner}/E_{matrix} = 2.0$ and Poisson's ratios are 0.3; the radii of outer and inner inhomogeneity are $0.2a_0$ and $0.15a_0$. Fig. 15 plots the equivalent plastic strains in the matrix when the double-layered inhomogeneity sets are at different locations. For all cases, the inhomogeneities lead to plastic strain concentrations, although the maximum values of ε_{Eq}^{P} vary from case to case.

For each plot in Fig. 15, the peak equivalent plastic strain in the matrix is found at one of the sides of the double-layered inhomogeneity (i.e. region I, II, or III, defined in Fig. 8(e)), whichever is the closest to the location of the maximum elastic stress of the homogeneous solution ($z = 0.48a_0$). For example, in Fig. 15(a), although the plastic strains concentrate in both region II and III, the magnitude of the equivalent plastic strain in region II is much higher than that in region III. On the contrary, when considering Fig. 15(c), the plastic strains tend to concentrate in region I because this region is closer to the maximum elastic stress of the corresponding homogeneous solution than to the lower region. Fig. 15(d) reveals that the maximum equivalent plastic strain in the left portion of region III of the double-layered inhomogeneity, which also follows the phenomena discussed above. These observations can also be viewed from another scenario. When the distances from any of those regions to the point of the maximum elastic stress of homogeneous solution are equal, i.e. the center of the double-layered inhomogeneity is situated at $(0, 0, 0.48a_0)$, the difference between

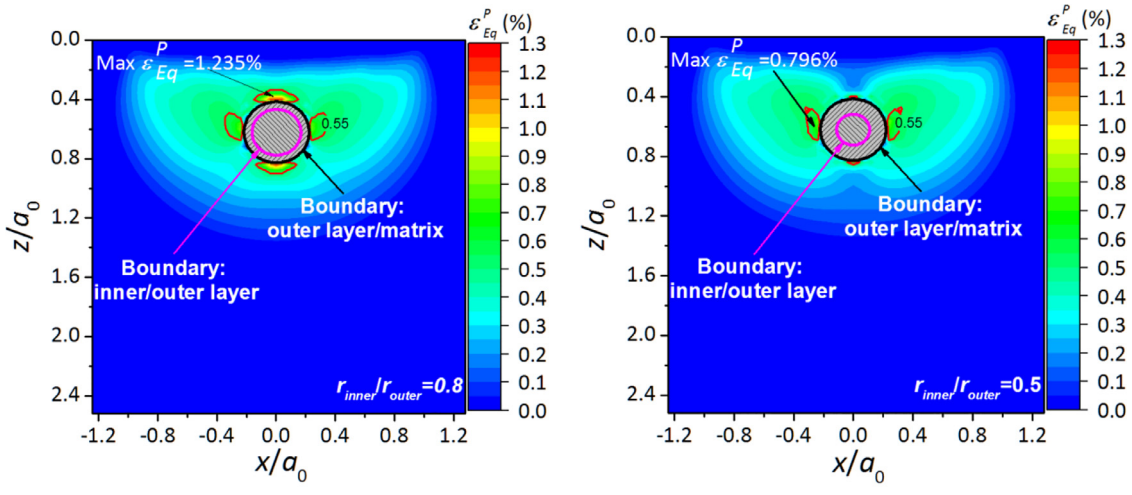

Fig. 12. Equivalent plastic strain fields in cross section XOZ, with varying size ratio of double-layered inhomogeneities: (a) $r_{inner}/r_{outer} = 0.8$ and (b) $r_{inner}/r_{outer} = 0.5$.

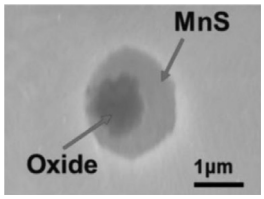

Fig. 13. A double-layered inhomogeneity in steel, where the inner and outer layers are not concentric (Zhang et al., 2016).

the global maximum and the secondary highest equivalent plastic strain is the minimum despite the non-uniform contact stress distribution of the homogeneous solution. As shown in Fig. 15(b), the global maximum of the equivalent plastic strain is 1.14%, while the value of the local maximum located in region III is 0.81%, thus the difference is 0.33%; and on the other hand, such differences in Fig. 15(a) and (c) are 0.48% and 0.38%, respectively.

Shape. The shape of inhomogeneities is commonly spherical or ellipsoidal. However, cuboidal inhomogeneities have also been observed in steels, as shown in Fig. 16. It is interesting to investigate the inhomogeneity shape effect on matrix material plasticity. In this section, the diameters of the inner and outer layers of a spherical inhomogeneity are $0.3a_0$ and $0.4a_0$, while the edge lengths of a cuboidal double-layered inhomogeneity are set to be $0.3a_0$ and $0.4a_0$. Young's moduli of the double-layered inhomogeneity set are $E_{outer}/E_{matrix} = 0.7$ and $E_{inner}/E_{matrix} = 2.0$, and Poisson's ratios are 0.3. Other parameters follow those used in Fig. 8. Fig. 17 plots the result comparisons, which are the plastic strain fields of matrix materials in section XOZ. Both inhomogeneities cause plastic strain concentrations in all three regions, but due to the sharp corners, the cuboidal inhomogeneity leads to larger plastic strain concentration regions and higher ε_{Eq}^{P} values than those of a spherical inhomogeneity, suggesting that cuboidal inhomogeneities could be more harmful.

3.2.3. Effect of inhomogeneity distributions

Multiple inhomogeneities may appear in a stringer, and each contributes to the imposed stresses and strains. The elastic analysis by Zhou et al., (2012) for the cases of two inhomogeneities indicates that their interaction becomes stronger when they are closer to each other. Amuzuga et al., (2016) studied the plastic strain

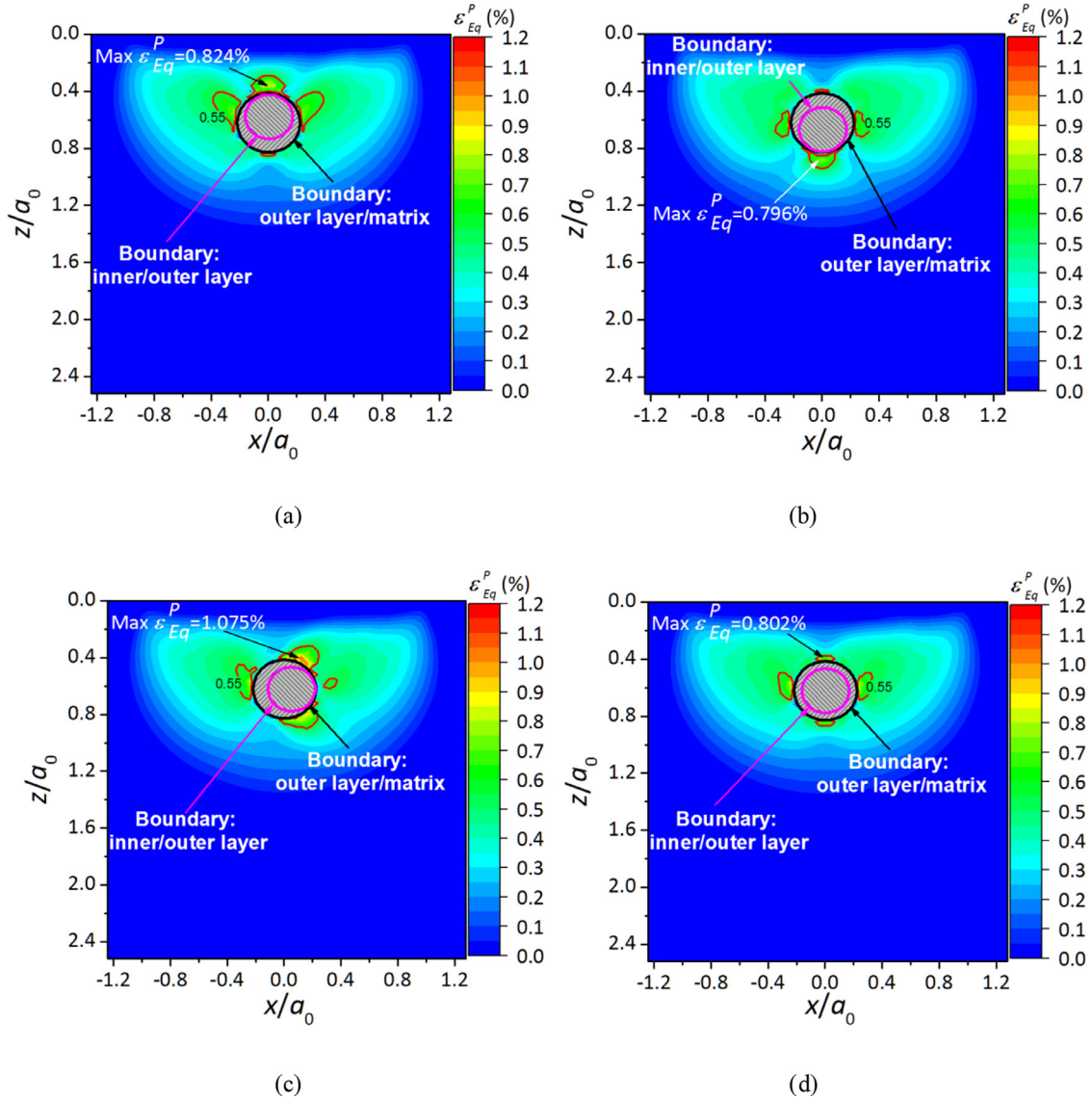

Fig. 14. Equivalent plastic strain fields in cross section XOZ, (a) (b) (c) with varying orentation of an eccentric double-layered inhomogeneity, and (d) a homocentric double-layered inhomogeneity.

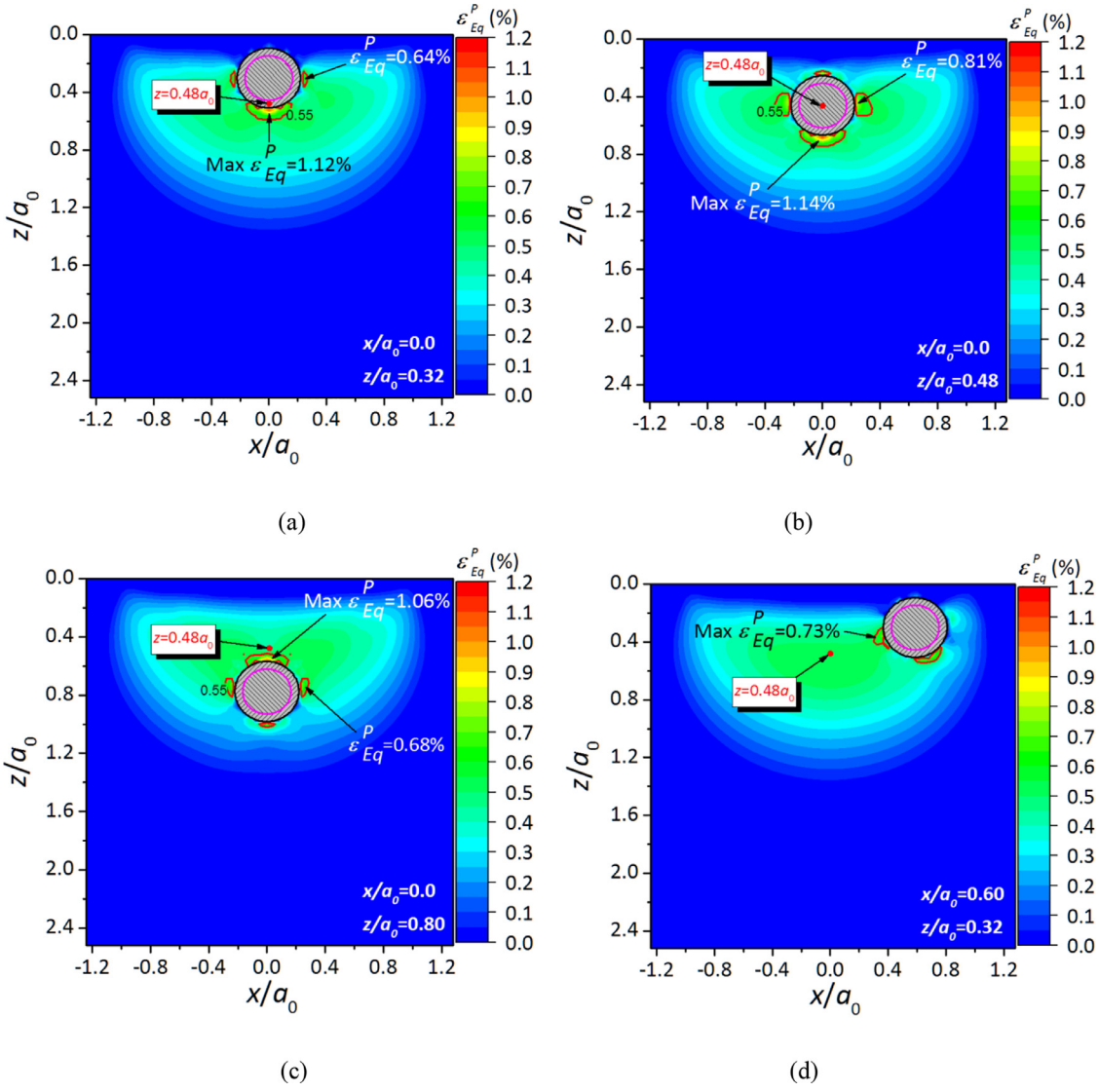

Fig. 15. Equivalent plastic strain fields in cross section XOZ of the maxtrix. The distances between the plastic strain concentration regions and the point of the maximum elastic stress from the homogeneous solution affect the plastic strain distribution.

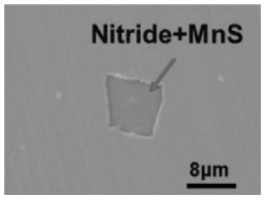

Fig. 16. A cuboidal inhomogeneity in steel (Zhang et al., 2016).

fields in the matrix material when a stringer of three uniform stiff inhomogeneities is involved. Their results indicated that the orientation of a stringer has a significant influence on the magnitudes of plastic strain concentration due to inhomogeneity interactions. This section studies the interaction between double-layered inhomogeneities, for which two double-layered inhomogeneities are arranged vertically or horizontally, one of them is centered (0, 0, $0.64a_0$) while the other moves along the x- or z-axis. Young's moduli of the double-layered inhomogeneity set are $E_{outer}/E_{matrix} = 0.7$ and $E_{inner}/E_{matrix} = 3.0$, and Poisson's ratios are both 0.3. Other parameters are chosen the same as those in Fig. 8(d).

The overlap of the plastic strain concentration regions is the key to understanding the effect of inhomogeneity distributions on plastic strain fields. As mentioned before, a double-layered inhomogeneity causes plastic strain concentration in region III. When two such inhomogeneities are horizontally spaced by a clearance as small as $d = 0.08a_0$ (Fig. 18(a)), their region III should overlap, hence resulting in the maximum plastic strain increase to 0.88%. However, the amplifying effect due to overlapping decreases when the two inhomogeneities are far away from each other. As shown in Fig. 18(b), when distance $d = 0.36a_0$, the inhomogeneities almost have no interaction because the sizes of plastic strain concentration regions are quite limited, as indicated by Fig. 10(b). The amplification effect due to overlapping can also be found in Fig. 18(c) as well, where the location of the maximum plastic strain (0.975%) is found in the narrow gap of $d = 0.04a_0$ between the vertically arranged inhomogeneities.

As stated in Fig. 8(b), a stiff inhomogeneity mainly causes plastic strain concentrated in region I and II, therefore, if spaced horizontally, these regions parallel to each other and will not be overlapped. This explains the phenomenon in a reference (Amuzuga et al., 2016), where a stiff inhomogeneity stringer vertical to the contact surface leads to the highest plastic strain in

Please cite this article as: M. Zhang et al., Elasto-plastic contact of materials containing double-layered inhomogeneities, International Journal of Solids and Structures (2017), http://dx.doi.org/10.1016/j.ijsolstr.2017.08.006

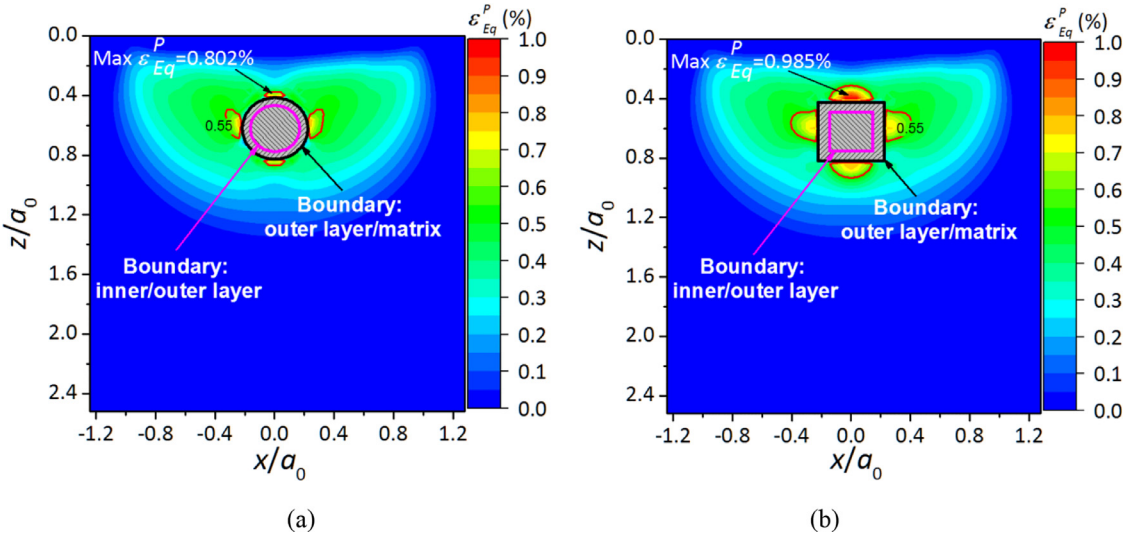

Fig. 17. Equivalent plastic strain fields in cross section XOZ, where (a) a spherical or (b) a cuboidal double-layered inhomgoeneity is involved.

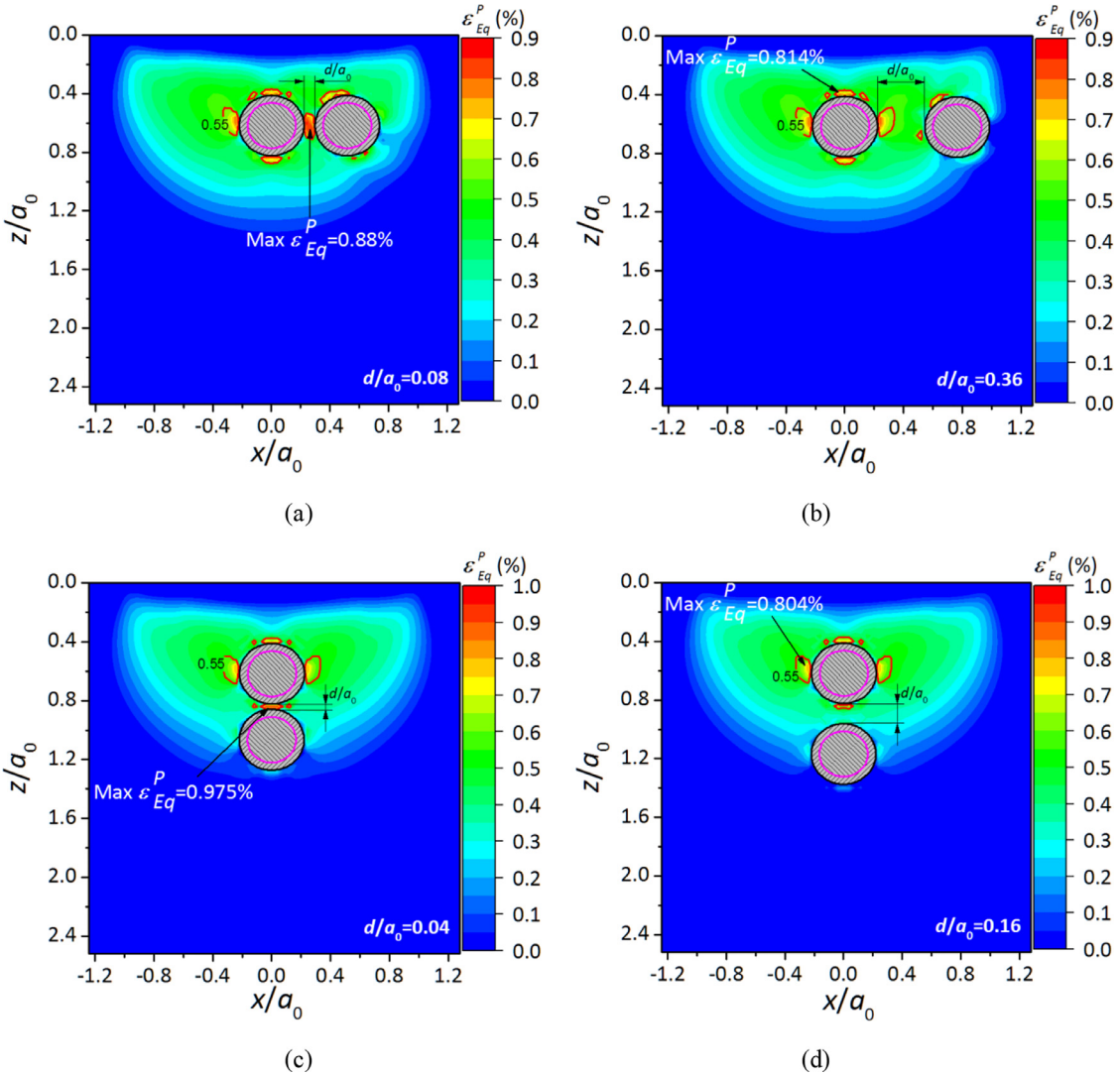

Fig. 18. Equivalent plastic strain fields in cross section XOZ. Two double-layered inhomogeneities are arranged vertically or horizontally to reveal the effect of inhomogeneity disributions on the matrix plasticity.

Please cite this article as: M. Zhang et al., Elasto-plastic contact of materials containing double-layered inhomogeneities, International Journal of Solids and Structures (2017), http://dx.doi.org/10.1016/j.ijsolstr.2017.08.006

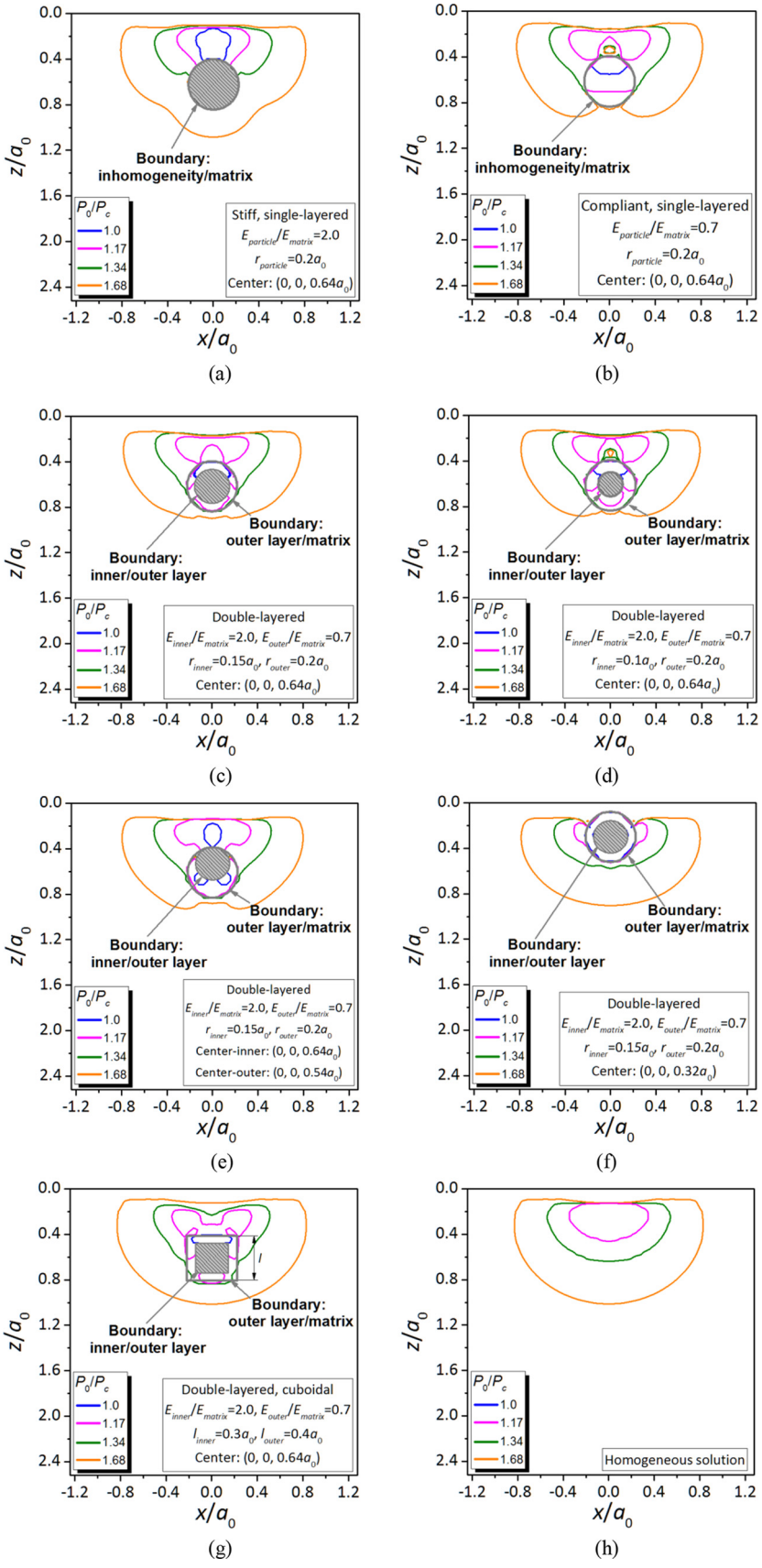

Fig. 19. Plastic region evolutions in section XOZ, (a–g) the half-sapce contains various types of inhomogeneity, and (h) the half-space is homogeneous.

comparison to other orientations. On the other hand, plastic strain concentration can only be found in region III around a uniform compliant inhomogeneity (Fig. 8(c)), suggesting that the horizontal stringers are more vulnerable for compliant inhomogeneities. However, a double-layered inhomogeneity may cause higher plastic strains in all three regions (depending on its material properties and geometric parameters, as discussed above), and it is highly possible that plastic strain concentrations be amplified by both horizontally and vertically lined double-layered inhomogeneities once they are very close to each other.

3.3. Initialization of yield

For a homogeneous half-space under a Hertzian contact, the maximum subsurface von Mises stress is approximate 0.62 times of the Hertz pressure P_0. Therefore, the critical load for the matrix material yield initialization in this study is $P_c = 1.18$ GPa corresponding to its yield strength set to be 0.73 GPa, as stated at the beginning of Section 3. The evolutions of the plastic regions are presented in Fig. 19. Seven representative cases are studied, which are a) uniform stiff inhomogeneity, b) uniform compliant inhomogeneity, c) double-layered inhomogeneity, d) double-layered inhomogeneity having a smaller core, e) double-layered inhomogeneity having an eccentric core, f) double-layered inhomogeneity in a different location, and g) cuboidal double-layered inhomogeneity. The plastic strain distributions in both the matrix and the outer inhomogeneity are plotted. The plastic strain field of the corresponding homogeneous case is given in h). Note that the compliant outer layer is elasto-plastic in all the double-layered cases of this paper, but in Sections 3.1 and 3.2, the plastic strains in the inhomogeneities were not plotted for clarity. Key parameters are listed in each figure.

In Fig. 19(a), plastic strains are found in the north polar region of the uniform stiff inhomogeneity even under the load of $P_0 = P_c$, which is, apparently, due to the stress concentrations caused by the stiff particle. For the case of uniform compliant inhomogeneity, plasticity starts from the upper boundary of the inhomogeneity and then extends along depth as the load increases. When the stiff particle is embedded in the compliant outer layer, as shown in Fig. 19(c) or (d), the plastic strain concentration induced by the core is confined within the double-layered inhomogeneity at first, and it then permeates to the matrix materials. In Fig. 19(e), the stiff core results in plastic strains in the matrix under critical load P_c because it is exposed to the matrix material without any buffer effect from an outer layer. Except what shown in Fig. 19(e), no plastic strain is found in the matrix material in other double-layered cases in Fig. 19 when $P_0 = P_c$, further demonstrating the buffer effect of the outer compliant layer, which more or less increases the critical load to cause matrix plastic deformation.

4. Conclusions

An elasto-plastic contact model, based on the numerical equivalent inclusion method, is presented for investigating the effects of double-layered inhomogeneity sets on the matrix plasticity of an inhomogeneity-containing material. The analyses were focused on the double-layered inhomogeneity of a stiff core enclosed by a compliant outer layer. The parameters of material properties, shape, and distribution of inhomogeneities were studied for their influences on the plastic strain concentrations measured by the maximum equivalent plastic strains. The results suggest following major findings:

- Increase in Young's modulus of the stiff inner layer can induce more serious plastic strain concentration in the upper and lower regions of the spherical double-layered inhomogeneity. Lowering Young's modulus of the compliant outer layer of the inhomogeneity makes it absorbs more plastic strain concentration caused by the stiff core.
- If the diameter of the inner stiff core is smaller than one half of that of the compliant outer layer, the double-layered inhomogeneity behaves like a uniform compliant inhomogeneity.
- For the cases of an individual double-layered inhomogeneity at different locations, the maximum equivalent plastic strain in the matrix is in one of the adjacent regions (upper, lower or equatorial) of the inhomogeneity, whichever is the closest to the location of the maximum elastic stress in the corresponding homogeneous material (which is $x = y = 0$ and $z = 0.48a_0$ in the current study).
- The eccentric inner stiff core in a double-layered inhomogeneity raises a higher plastic strain concentration than does a concentric one. In addition, a cuboidal double-layered inhomogeneity causes stronger plastic strain concentration in the matrix than does a spherical one.
- For the cases of multiple double-layered inhomogeneities, the overlap of the plastic strain concentration regions, either vertically or parallel to the loading surface, amplifies the plasticity disturbance caused by the double-layered inhomogeneities.
- If the stiff core of a double-layered inhomogeneity is completely encircled by the outer layer, plastic strains should initiate from the compliant outer layer and then permeate into the matrix material. The compliant outer layer provides a buffering function.

Acknowledgements

The authors would like to thank TimkenSteel for research support. M. Zhang would also like to thank the scholarship support from China Scholarship Council (grant number 201406290097). M. Zhang, Q. Wang, and L. M. Keer would also like to acknowledge the support from US National Science Foundation (CMMI-1434834). Center for Surface Engineering and Tribology at Northwestern University, Evanston, USA, is also acknowledged.

References

Amuzuga, K., Chaise, T., Duval, A., Nelias, D., 2016. Fully coupled resolution of heterogeneous elastic–plastic contact problem. J. Tribol. 138, 21403.
Atkinson, H., Shi, G., 2003. Characterization of inclusions in clean steels: A review including the statistics of extremes methods. Prog. Mater. Sci. 48, 457–520.
Bhattacharyya, A., Subhash, G., Arakere, N., 2014. Evolution of subsurface plastic zone due to rolling contact fatigue of M-50 NiL case hardened bearing steel. Int. J. Fatigue 59, 102–113.
Byun, J.S., Shim, J.H., Cho, Y.W., Lee, D.N., 2003. Non-metallic inclusion and intragranular nucleation of ferrite in Ti-killed C-Mn steel. Acta Mater 51, 1593–1606.
Chang, C., Jung, I., Park, S., Kim, H., Lee, H., 2005. Effect of Mg on the evolution of non-metallic inclusions in Mn–Si–Ti deoxidised steel during solidification: experiments and thermodynamic calculations. Ironmak. Steelmak. 32, 251–257.
Chen, W., Liu, S., Wang, Q., 2008. Fast fourier transform based numerical methods for elasto-plastic contacts of nominally flat surfaces. J. Appl. Mech. 75, 11022.
Dong, Q., Zhou, K., Chen, W., Fan, Q., 2016. Partial slip contact modeling of heterogeneous elasto-plastic materials. Int. J. Mech. Sci. 114, 98–110.
Eshelby, J., 1957. The determination of the elastic field of an ellipsoidal inclusion, and related problems. Proc. R. Soc. A Math. Phys. Eng. Sci.
Fatemi, A., Socie, D., 1988. Critical plane approach to multiaxial fatigue damage including out-of-phase loading. Fatigue Fract. Eng. Mater. Struct. 11, 149–165.
Fotiu, P., Nemat-Nasser, S., 1996. A universal integration algorithm for rate-dependent elastoplasticity. Comput. Struct. 59, 1173–1184.
Gao, X., Jing, X., Subhash, G., 2006. Two new expanding cavity models for indentation deformations of elastic strain-hardening materials. Int. J. Solids Struct. 43, 2193–2208.
Hashimoto, K., Fujimatsu, T., Tsunekage, N., Hiraoka, K., Kida, K., Santos, E.C., 2011. Study of rolling contact fatigue of bearing steels in relation to various oxide inclusions. Mater. Des. 32, 1605–1611.
Jacq, C., Nelias, D., Lormand, G., Girodin, D., 2002. Development of a three-dimensional semi-analytical elastic-plastic contact code. J. Tribol. 124, 653.
Koumi, K., Zhao, L., Leroux, J., Chaise, T., Nelias, D., 2014. Contact analysis in the presence of an ellipsoidal inhomogeneity within a half space. Int. J. Solids Struct. 51, 1390–1402.
Leroux, J., Fulleringer, B., Nélias, D., 2010. Contact analysis in presence of spherical inhomogeneities within a half-space. Int. J. Solids Struct. 47, 3034–3049.

Please cite this article as: M. Zhang et al., Elasto-plastic contact of materials containing double-layered inhomogeneities, International Journal of Solids and Structures (2017), http://dx.doi.org/10.1016/j.ijsolstr.2017.08.006

Li, S., 2012. Effects of inclusions on very high cycle fatigue properties of high strength steels. Int. Mater. Rev. 57, 92–114.
Li, W., Wang, P., Lu, L., Sakai, T., 2014. Evaluation of gigacycle fatigue limit and life of high-strength steel with interior inclusion-induced failure. Int. J. Damage Mech. 23, 931–948.
Lis, T., 2009. Modification of oxygen and sulphur inclusions in steel by calcium treatment. Metalurgija 48, 95–98.
Liu, S., Hua, D., Chen, W., Wang, Q., 2007. Tribological modeling: Application of fast Fourier transform. Tribol. Int. 40, 1284–1293.
Liu, S., Jin, X., Wang, Z., Keer, L., Wang, Q., 2012. Analytical solution for elastic fields caused by eigenstrains in a half-space and numerical implementation based on FFT. Int. J. Plast. 35, 135–154.
Liu, S., Wang, Q., 2005. Elastic fields due to eigenstrains in a half-space. J. Appl. Mech. 72, 871–878.
Liu, S., Wang, Q., 2002. Studying contact stress fields caused by surface tractions with a discrete convolution and fast fourier transform algorithm. J. Tribol. 124, 36–45.
Liu, S., Wang, Q., Liu, G., 2000. A versatile method of discrete convolution and FFT (DC-FFT) for contact analyses. Wear 243, 101–111.
Lu, L., Zhang, J., Shiozawa, K., 2009. Influence of inclusion size on S-N curve characteristics of high-strength steels in the giga-cycle fatigue regime. Fatigue Fract. Eng. Mater. Struct. 32, 647–655.
Luo, S., Su, Y., Lu, M., Kuo, J., 2013. EBSD analysis of magnesium addition on inclusion formation in SS400 structural steel. Mater. Charact. 82, 103–112.
Matsuno, F., Nishikida, S., Ikesaki, H., 2006. Mechanical properties of manganese sulphides in the temperature range between room temperature and 1000.DEG.C. Isij Int. 25, 989–998.
Moghaddam, S., Sadeghi, F., 2016. A review of microstructural alterations around nonmetallic inclusions in bearing steel during rolling contact fatigue. Tribol. Trans. 59, 1142–1156.
Moghaddam, S., Sadeghi, F., Paulson, K., Weinzapfel, N., Correns, M., Bakolas, V., Dinkel, M., 2015. Effect of non-metallic inclusions on butterfly wing initiation, crack formation, and spall geometry in bearing steels. Int. J. Fatigue 80, 203–215.
Moghaddam, S., Sadeghi, F., Weinzapfel, N., Liebel, A., 2014. A damage mechanics approach to simulate butterfly wing formation around nonmetallic inclusions. J. Tribol. 137, 11404.
Mura, T., 1987. Micromechanics of Defects in Solids, Mechanics of Elastic and Inelastic Solids. Martinus Nijhoff, Dordrecht.
Murakami, Y., 2002a. Bearing Steels. In: Murakami, Y. (Ed.), Metal Fatigue. Elsevier Science Ltd, Oxford, pp. 129–162. Chapter 7.
Murakami, Y., 2002b. Effect of Size and Geometry of Small Defects on the Fatigue Limit. In: Murakami, Y. (Ed.), Metal Fatigue. Elsevier Science Ltd, Oxford, pp. 35–55. Chapter 4.
Nelías, D., Boucly, V., Brunet, M., 2006. Elastic-plastic contact between rough surfaces: proposal for a wear or running-in model. J. Tribol. 128, 236.
Pandkar, A., Arakere, N., Subhash, G., 2014. Microstructure-sensitive accumulation of plastic strain due to ratcheting in bearing steels subject to Rolling Contact Fatigue. Int. J. Fatigue 63, 191–202.
Polonsky, I., Keer, L., 1999. A numerical method for solving rough contact problems based on the multi-level multi-summation and conjugate gradient techniques. Wear 231, 206–219.
Przybyla, C., Prasannavenkatesan, R., Salajegheh, N., McDowell, D., 2010. Microstructure-sensitive modeling of high cycle fatigue. Int. J. Fatigue 32, 512–525.
Sun, C., Lei, Z., Xie, J., Hong, Y., 2013. Effects of inclusion size and stress ratio on fatigue strength for high-strength steels with fish-eye mode failure. Int. J. Fatigue 48, 19–27.
Wang, Z., Jin, X., Keer, L., Wang, Q., 2013a. Novel model for partial-slip contact involving a material with inhomogeneity. J. Tribol. 135, 41401.
Wang, Z., Jin, X., Zhou, Q., Ai, X., Keer, L., Wang, Q., 2013b. An efficient numerical method with a parallel computational strategy for solving arbitrarily shaped inclusions in elastoplastic contact problems. J. Tribol. 135, 31401.
Yu, H., Sanday, S., 1991. Elastic fields in joined half-spaces due to nuclei of strain. Proc. R. Soc. A Math. Phys. Eng. Sci. 434, 503–519.
Zhang, J., Li, S., Yang, Z., Li, G., Hui, W., Weng, Y., 2007. Influence of inclusion size on fatigue behavior of high strength steels in the gigacycle fatigue regime. Int. J. Fatigue 29, 765–771.
Zhang, J., Lu, L., Wu, P., Ma, J., Wang, G., Zhang, W., 2013. Inclusion size evaluation and fatigue strength analysis of 35CrMo alloy railway axle steel. Mater. Sci. Eng. A 562, 211–217.
Zhang, J., Zhang, J., Yang, Z., Li, G., Yao, G., Li, S., Hui, W., Weng, Y., 2005. Estimation of maximum inclusion size and fatigue strength in high-strength ADF1 steel. Mater. Sci. Eng. A 394, 126–131.
Zhang, M., Neu, R., McDowell, D., 2009. Microstructure-sensitive modeling: Application to fretting contacts. Int. J. Fatigue 31, 1397–1406.
Zhang, X., Zhang, L., Yang, W., Dong, Y., 2016. Characterization of MnS particles in heavy rail steels using different methods. Steel Res. Int. 87, 1–16.
Zhou, K., Chen, W., Keer, L., Ai, X., Sawamiphakdi, K., Glaws, P., Wang, Q., 2011. Multiple 3D inhomogeneous inclusions in a half space under contact loading. Mech. Mater. 43, 444–457.
Zhou, K., Hoh, H., Wang, X., Keer, L., Pang, H., Song, B., Wang, Q., 2013. A review of recent works on inclusions. Mech. Mater. 60, 144–158.
Zhou, K., Keer, L., Wang, Q., Ai, X., Sawamiphakdi, K., Glaws, P., Paire, M., Che, F., 2012. Interaction of multiple inhomogeneous inclusions beneath a surface. Comput. Methods Appl. Mech. Eng. 217–220, 25–33.
Zhou, Q., Jin, X., Wang, Z., Wang, J., Keer, L., Wang, Q., 2015. Numerical implementation of the equivalent inclusion method for 2D arbitrarily shaped inhomogeneities. J. Elast. 118, 39–61.
Zhou, Q., Jin, X., Wang, Z., Wang, J., Keer, L., Wang, Q., 2014a. An efficient approximate numerical method for modeling contact of materials with distributed inhomogeneities. Int. J. Solids Struct. 51, 3410–3421.
Zhou, Q., Xie, L., Jin, X., Wang, Z., Wang, J., Keer, L., Wang, Q., 2014b. Numerical modeling of distributed inhomogeneities and their effect on rolling-contact fatigue life. J. Tribol. 137, 11402.

Please cite this article as: M. Zhang et al., Elasto-plastic contact of materials containing double-layered inhomogeneities, International Journal of Solids and Structures (2017), http://dx.doi.org/10.1016/j.ijsolstr.2017.08.006